2022-12-12

Single-Shot, Ultrafast, Multi-Frame X-Ray Imaging of Defect-Bearing Ablator Materials in Extreme Conditions

Daniel S. Hodge
Brigham Young University

Single-Shot, Ultrafast, Multi-Frame X-Ray Imaging of Defect-Bearing Ablator Materials in Extreme Conditions

Daniel S. Hodge

A thesis submitted to the faculty of
Brigham Young University
in partial fulfillment of the requirements for the degree of

Master of Science

Richard L. Sandberg, Chair
Benjamin Frandsen
Justin Peatross

Department of Physics and Astronomy

Brigham Young University

ABSTRACT

Single-Shot, Ultrafast, Multi-Frame X-Ray Imaging of Defect-Bearing Ablator Materials in Extreme Conditions

Daniel S. Hodge
Department of Physics and Astronomy, BYU
Master of Science

Characterization of the dynamic behavior of defect-bearing ablator materials subjected to extreme conditions is essential in advancing fusion energy as an reliable and abundant energy source. By understanding how materials evolve spatially and temporally we can minimize hydrodynamic instabilities, which are major contributing factors to energy yield degradation in inertial confinement fusion (ICF) experiments. In this thesis we demonstrate the capabilities of an ultrafast x-ray imaging (UXI) detector, the Icarus V2, where we capture multiple frames of single void-bearing sample compressed by a high-intensity laser shockwave. Using the Matter in Extreme Conditions (MEC) instrument at the Linac Coherent Light Source (LCLS), we conducted two experiments with the x-ray free electron laser (XFEL) multi-pulse mode, delivering four nanosecond-separated pulses to a sample impacted by a laser shockwave, obtaining multiframe images of a single sample in the holographic and direct imaging regime with the UXI detector. In contrast to the low temporal resolution provided by current cameras, the Icarus V2 can capture images with high temporal resolution, which can be used to determine the mechanisms that prevent thermonuclear ignition in ICF experiments. For images captured in the holographic regime at our XFEL energy of 8.23 keV, we realized that the shock front was obscured by strong phase-contrast effects. We recognized that by increasing the XFEL energy while in the holographic regime, more distinguishable features could be revealed behind and along the shock front. Alternatively, in the direct-imaging configuration we discovered that the evolution of microstructural features were directly recognizable in comparison to the holographic regime at lower XFEL energies. Overall, the images captured by the UXI in both regimes demonstrated our ability to obtain multiframe images of processes that occur over several nanoseconds for single samples, which has never been done before. Moreover, the capabilities of the UXI enable extraction of quantitative information over multiple frames, which can help with uncovering the underlying physics involved in high energy density (HED) physics experiments and other experiments involving non-repeatable ultrafast phenomena. Specifically, insight into the behavior of the void can be gained by performing phase retrieval on the images and obtaining the areal density of the materials during laser-shock ablation. Generally, the UXI improves data acquisition speed and operational efficiency, which extends this camera's functionality to experiments that occur at various time scales or experiments that require multiple images to be captured.

Keywords: ultrafast, x-ray, imaging, shock, void, Icarus V2, UXI, MEC, pulse, void-shock, heterogeneities, inhomogeneities, fusion, XFEL

ACKNOWLEDGMENTS

I would like to express my gratitude to Professor Richard L. Sandberg. I have been lucky to have an advisor who has cared about my continual growth and work. Moreover, I am grateful for his insights, perspectives, and support over the past couple years. I also wanted to express my appreciation to the undergraduate and graduate students with whom I have collaborated. In particular, I am grateful for Taylor Buckway, Nick Porter, Jason Meziere, Mathew Ricks, and Christian McCombs and their insights and contributions. Last, but not least, I want to thank my family for their encouragement and support these past few years.

Contents

List of Figures

List of Tables

Chapter 1

Introduction

1.1 Motivation: Inertial confinement fusion (ICF)

Inertial confinement fusion (ICF) was introduced by Nuckolls [1] in 1972 as a promising method that has the potential to generate a vast amount of energy from a small fuel target, yielding cleaner and more abundant energy than modern sources. Additionally, as compared to nuclear fission based methods, the fuel for fusion can be refined from ocean water, making it clean and abundant. ICF is a process which involves high-intensity lasers dynamically compressing a fuel target, which in turn increases the temperature and density of the fuel, initiating thermonuclear ignition. This process is illustrated in Fig. 1.1.

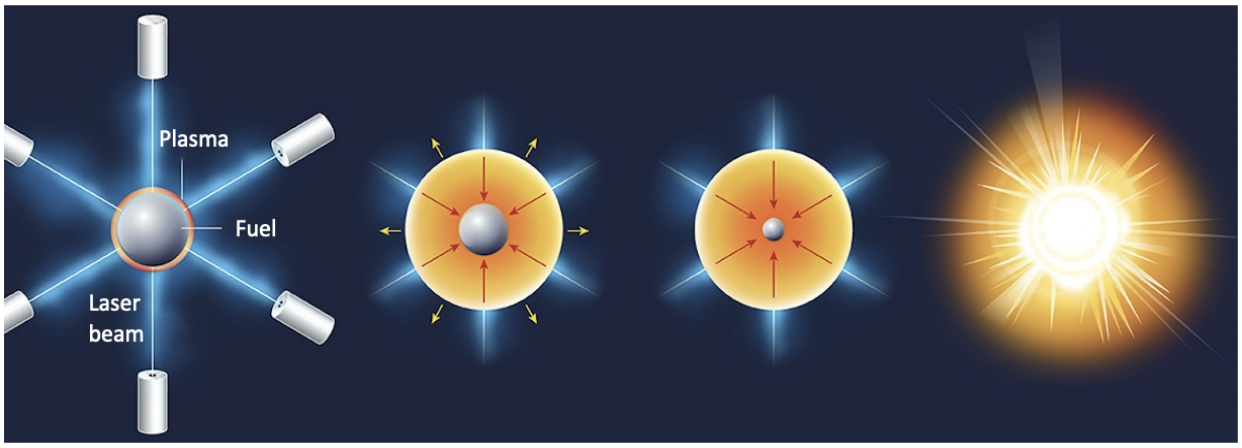

Figure 1.1 The image provided here was taken from Herrmann et al. [2] and it illustrates the processes that occur in ICF experiments. Multiple lasers are used to rapidly heat the ablator shell (∼mm in diameter) producing a plasma. The yellow arrows show the plasma that is imploding outwards, followed by large inward forces (red arrows) that compress the fuel. The compression causes an increase in temperature and pressure, heating up the fuel and ignition occurs.

Although simple in concept, achieving successful fusion ignition requires a high degree of uniformity and symmetry [3], requiring a material without imperfections or voids. This stipulation is impractical since voids and imperfections are naturally-occurring in common ICF ablators, such as glow discharge polymer, high density carbon, and sputtered beryllium [4–7], resulting in a degradation of energy yield in current ICF experiments [8]. Several mechanisms [8–10] have prevented high energy yield, motivating the necessity for imaging shocked material instabilities at the nanoscale and understanding how its structure evolves spatially and temporally.

Evidence exists that internal inhomogeneities, such as defects and voids in the ablator shell, is the primary cause of instabilities in ICF experiments. Namely, Rayleigh-Taylor (RT) and Richtmyer-Meshkov (RM) instabilities, prevent symmetry of compression and produces low energy yield [8, 11]. The RT instability occurs during the ablation phase in the fusion process (second panel in Fig 1.1). The surface imperfections grow when a low density ablated material is accelerated toward high density material, progressively increasing distortion effects at the interface of these two

materials [12–14]. As the ablator-fuel interface continues to be compressed, the instability growth amplifies, causing the imploding shock to deviate from spherical [15]. Moreover, this causes the perturbation information to be carried through the ablator shell and rippling the interface between ablator and fuel [15]. This instability is illustrated in panels (a) and (b) in Fig. 1.2. The resulting outcome is a premature, turbulent mixing that lowers the density and temperature essential for fusion ignition. This dynamic process is the most dominant instability and occurs because these two fluids seek to minimize their combined potential energy [12–14].

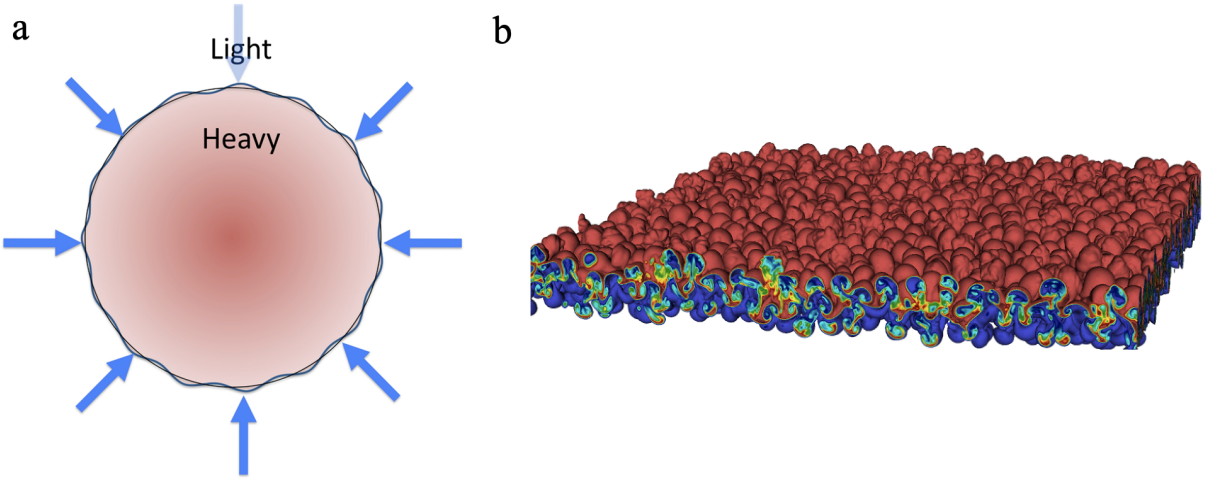

Figure 1.2 The image and simulation provided here were taken from [16]. **a:** Diagram depicting the RT instability at the fuel-ablator interface where the light ablator shell is pushing on the denser, heavier fuel. **b:** 3D simulation of the RT instability created by Lawrence Livermore National Laboratory (LLNL) using the *Miranda* code [16]. This simulation displays a zoomed in version of what we would expect to see at surface of the material shown in (a) when a light ablator shell pushes on dense fuel. Red indicates regions of higher temperature, blue indicates regions of lower temperature, and the other colors indicate regions of mixed temperature. The presence of varied temperatures contributes to the RT instability.

The RM instability is viewed as the impulsive counterpart of the RT instability [17, 18]. When a high pressure shock wave impulsively accelerates a perturbed interface between two fluids [18], the RM instability is created. Although RT and RM instabilities occur in different physical circumstances and stages in the implosion process, they have similar features in their evolution

and can interact with each other, causing non-linear mixing and "jetting" of the material, further preventing successful fusion ignition [15, 19–21]. The effect of both RM and RT instabilities can be seen in Fig. 1.3. The densities displayed in this simulation indicate that the density is widely distributed due to these instabilities.

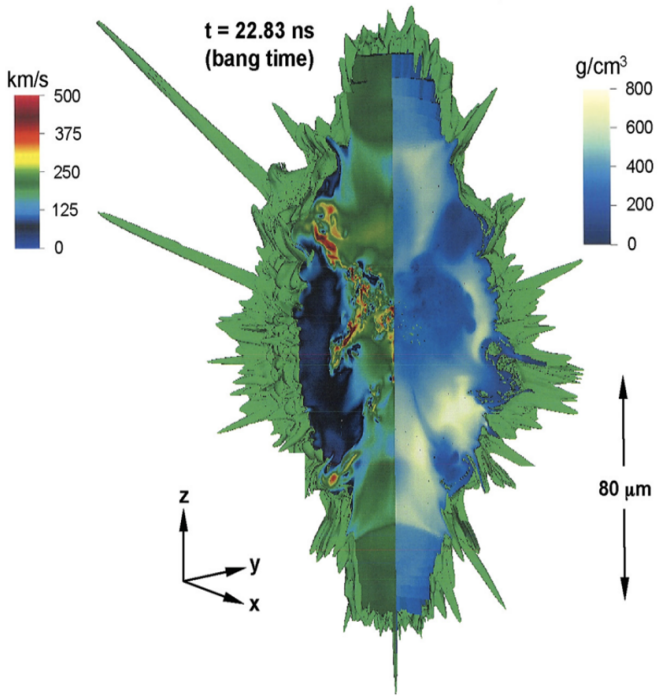

Figure 1.3 The image provided here is a 3D simulation of the ICF implosion which was taken from Clark et al. [19]. This image is split into two parts: (1) The left portion of the image displays the fluid flow speeds. Blue regions indicate slower speeds while red regions indicate faster speeds. (2) The right portion of the image illustrates how instabilities can affect the implosion of the fuel target. The color bar displayed here shows how the density is not uniform, initiating the perturbations that are protruding outwards.

Therefore, characterization of ablator materials and their physical and chemical composition during shock compression is essential to maximize energy output for ICF experiments — a necessary condition to enable fusion energy as an abundant energy source. Imaging techniques can be used to determine the asymmetries and instability growth that arises during compression due to voids or

imperfections within the ablator material. Although recent advancements have been made toward fusion energy [22], further exploration is required into how defects and voids alter the fusion energy process and produce low energy yield.

1.2 Areal density for void-shock interactions

Currently simulations, such as the one shown in Fig. 1.3, indicate that jetting and other undesirable features arise when instabilities such as RT and RM are present during laser ablation. To determine if these simulated predictions are accurate and to quantify how voids impact ablator performance during laser shock compression requires knowledge of the dynamic evolution of the density of the sample as the shockwave interacts with the void. This is challenging to determine due to the need for high resolution (sub-micron) imaging and ultrafast time scales. One possible solution is to image these samples with coherent x-ray imaging (CXI) techniques to extract the areal density of a sample (see Chapters 2 and 3). The areal density, in units of g/cm^2, is defined as the line-integrated mass density $\sigma(x,y)$. In literature [10, 19, 23], it is usually expressed as

$$\sigma(x,y) = \int_0^R \rho(x,y,z)\,dz \tag{1.1}$$

where $\rho(x,y,z)$ is the density of the sample in units of g/cm^3, R is the thickness of the sample in units of cm along the x-ray propagation direction, and the integration is carried out over the extent of the sample along the optical axis. Areal density is a key performance parameter for ICF science that informs us about the quality of compression or implosion [10].

When retrieving areal density from intensity images captured in the x-ray regime, it is necessary to consider the complex refractive index. This relation is expressed as

$$n(x,y,z) = 1 - \delta(x,y,z) + i\beta(x,y,z). \tag{1.2}$$

The decrement to unity δ is the real part of the refractive index that describes the changes in the wave's velocity due to oscillations of free and bound electrons, which leads to wavefront phase variations as the x-ray wave propagates through a material. β is the imaginary part of the refractive index that describes the absorption of a material. The parameters x and y describe the transverse dimensions of the sample, and z describes the propagation direction of the x-rays. When considering x-ray energies away from absorption edges, δ and β are expressed as functions of the electron density $\rho(x,y,z)$ as [24]

$$\delta(x,y,z) = \frac{\rho(x,y,z) r_e \lambda^2}{2\pi} \tag{1.3}$$

and

$$\beta(x,y,z) = \frac{\mu(x,y,z)\lambda}{4\pi}, \tag{1.4}$$

where r_e is the classical electron radius (2.82×10^{-15} m), λ is the x-ray wavelength, and $\mu(x,y,z)$ is the linear attenuation coefficient in units of inverse length. The last quantity required for areal density extraction is the phase $\Phi(x,y)$ of the sample's exit surface wave (ESW) and its relation to the refractive index $n(x,y,z)$. This relation is expressed as

$$\Phi(x,y) = -k \int \delta(x,y,z)\, dz, \tag{1.5}$$

with k as the wave vector. The integral is performed along the propagation direction of the x-rays. By inserting Eq. 1.3 into Eq. 1.5 and simplifying the expression we are left with

$$\frac{-\Phi(x,y)}{\lambda r_e} = \int \rho(x,y,z)\, dz, \tag{1.6}$$

which is the projected electron density. Equation 1.6 shows that the phase Φ is mandatory to determine areal density. Hence, there is a requirement to retrieve the phase map Φ of an illuminated

sample. However, in experiment, phase information is lost because electromagnetic radiation (i.e., x-rays) oscillates too rapidly for modern detectors to capture the phase and only intensity is recorded. Thus, techniques are implemented to recover the phase (phase retrieval) from intensity patterns (see Sec. 4.1). Discussion about CXI and the various phase retrieval methods are in Sec. 4.1. With these methods, we can generate a phase map that corresponds to our sample, which can then be used to determine the density distribution of our sample, yielding insights into why instabilities form when a compressive wave impacts a void within an ablator material.

1.3 LCLS XFEL and implementation of the UXI camera

With advances in coherent and brilliant hard x-ray sources, such as the Linac Coherent Light Source (LCLS) x-ray free electron laser (XFEL) [25–28], we can image nanoscale materials in these extreme states: 1) high pressures (GPa), 2) high temperatures (1000's of Kelvin), and 3) x-ray radiation environments (up to 25 keV [28]). This makes XFELs particularly valuable for high energy density (HED) physics experiments since these extreme conditions are involved. Hard x-rays generated by an XFEL are beneficial because we can view the internal structure of dense materials or plasmas, even when materials are dynamically changing. Additionally, XFELs enable high temporal resolution with x-ray pulse lengths as short as a few femtoseconds [28], enabling time-resolved measurements that are unattainable by other modern x-ray sources. This aspect of XFELs is applicable to many physics experiments and applications since many fundamental interactions happen over this timescale [27, 28], thereby making XFELs an ideal tool for studying dynamic phenomena and single-shot imaging. The general functionality of an XFEL is shown in Fig. 1.4.

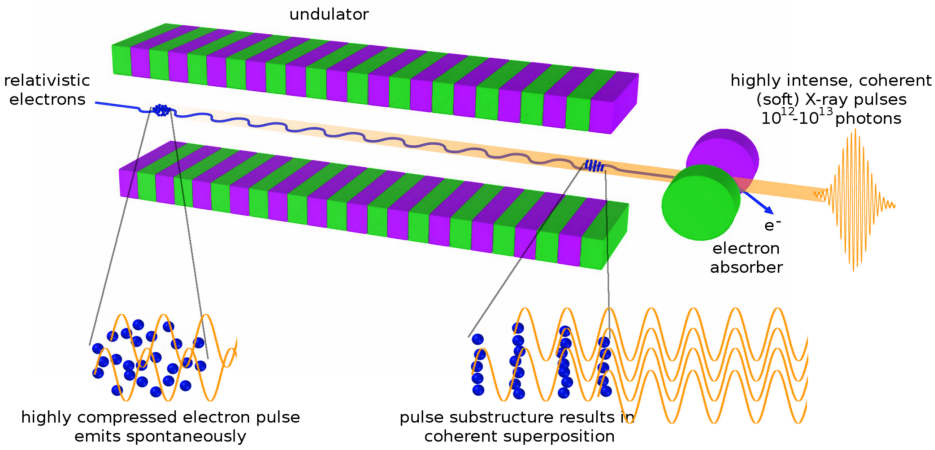

Figure 1.4 A diagram depicting the functionality of XFELs from [29]. Initially, a compressed electron bunch is accelerated to relativistic velocities and radiates incoherent spontaneous radiation. As the electrons pass through an undulator they emit radiation that retroactively acts on the electron bunch [30], separating it into micro bunches which emits a brilliant, femtosecond pulse of highly coherent x-ray radiation.

As previously stated in Sec. 1.1, the dynamic phenomena of interest are the instabilities that arise when a high-intensity laser compresses a target that contains inhomogeneities such as voids. One of the several places that we can investigate how these instabilities evolve is at the LCLS. One particular advantage that the LCLS provides over other facilities is its multi-pulse mode [31, 32], where up to eight pulses separated by a few nanoseconds between each pulse can be used to illuminate a sample [31–33]. The first experiments utilizing the multi-pulse mode were performed by Hart et al. [33] where they used two-pulse bunches separated by 4.2 ns to determine microstructure-to-nanostructure changes of a single copper target. To capture the evolving copper structure they used an UXI camera, the Icarus V1, to record two frames of a single target. This was the first time where the combination of an UXI detector and multi-pulse mode were implemented.

In experiments presented in this thesis, we use a high-intensity laser shockwave at the MEC at LCLS to compress a more complicated sample (hollow glass bubble inside a plastic ablator material), resembling voids commonly seen in ICF experiments [34]. During compression we

illuminated this single sample with four pulses generated by the LCLS multi-pulse mode. We utilized the Icarus V2, an UXI camera, to record multiframe images of a single void-bearing ablator material during compression, enabling visualization of microstructural features that alter over nanosecond time scales. The details about the UXI and its capability are demonstrated in Chapter 2 and Chapter 3, which are two manuscripts submitted to different journals. These manuscripts present novel experiments involving the Icarus V2 camera, which enables us to peer at timescales that have previously not been achievable, yielding insight into multi-material behavior on ICF-relevant time scales.

Chapter 2

Initial UXI results captured in the holographic regime

Below is the text from a manuscript submitted to the SPIE journal titled, **"Visualization of Shocked Material Instabilities Using a Fast-Framing Camera and XFEL Four-Pulse Train"** by D. S. Hodge, S. Pandolfi, Y. Liu, K. Li, A. Sakdinawat, M. Seaberg, P. Hart, E. Galtier, D. Khaghani, S. Vetter, F. J. Decker, B. Nagler, H. J. Lee, C. Bolme, K. Ramos, P. M. Kozlowski, D. S. Montgomery, T. Carver, M. Dayton, L. Dresselhaus-Marais, S. Ali, R. L. Sandberg, A. E. Gleason [35].

Abstract. Many questions regarding dynamic materials could be answered by using time-resolved ultra-fast imaging techniques to characterize the physical and chemical behavior of materials in extreme conditions and their evolution on the nanosecond scale. In this work, we perform multi-frame phase-contrast imaging (PCI) of micro-voids in low density polymers under laser-driven shock compression. At the Matter in Extreme Conditions (MEC) Instrument at the Linac Coherent Light Source (LCLS), we used a train of four x-ray free electron laser (XFEL) pulses to probe the evolution of the samples. To visualize the void and shock wave interaction, we deployed the Icarus V2 detector to record up to four XFEL pulses, separated by 1-3 nanoseconds. In this work, we image elastic waves interacting with the micro-voids at a pressure of several GPa. Monitoring how the material's heterogeneities, like micro-voids, dictate its response to a compressive wave is important for benchmarking the performances of inertial confinement fusion energy materials. For the first time in a single sample, we have combined an ultrafast x-ray framing camera and four XFEL pulse train to create an ultrafast movie of micro-void evolution under laser-driven shock compression. Eventually, we hope this technique will resolve the material density as it evolves dynamically under laser shock compression.

2.1 Introduction

Studying transient behavior of matter in extreme conditions is vital to the understanding of the physical and chemical processes found in materials and in nature [36–41]. Imperfections at the micron scale influence the physical and chemical behavior of all materials, and it is thus crucial to understand how structural defects alter the materials response to extreme conditions. For example, it has been proposed that the growth of hydrodynamic instabilities, such as the Rayleigh-Taylor (RT) and Richtmeyer-Meshkov (RM) instabilities, at present, prevents thermonuclear ignition in inertial confinement fusion (ICF) tests [3, 4, 8, 19]. These instabilities along with implosion asymmetries contribute significantly to the degradation of materials performance in ICF implosions [3, 19]. During recent experiments at the National Ignition Facility (NIF), degradation was observed when high-density carbon (HDC) ablator material mixed with the hot spot during the implosion, resulting in "meteors" or bright spots in x-ray images [4, 8]. It has been suggested that the occurrence of these "meteors" might be caused by the presence of micro-voids in the HDC layer. Therefore, being able to image dynamic events at the critical nanosecond and sub-micron scale is important to understand the interaction of shock waves with structural defects, as they may play a crucial role in the seeding and growth of hydrodynamic instabilities that currently prevent ignition in ICF experiments.

To analyze how instabilities arise in shock-void interactions, we combined the four-pulse XFEL mode at LCLS, the Icarus V2 ultrafast x-ray imaging (UXI) camera, and laser-shock compression at the MEC instrument to analyze the evolution of microstructural heterogeneities under nanosecond laser-driven shock compression. In our experiment, an optical long-pulse laser produces shock waves that interact with a hollow silica shell void embedded in photoresist polymer SU-8 samples. To

examine material performance in these extreme states, we used the LCLS XFEL four-pulse train and the Icarus V2 camera to collect x-ray phase-contrast images. The Icarus V2 detector is an ultrafast x-ray imaging (UXI) camera developed by Sandia and Lawrence Livermore National Laboratories for the study of high energy density physics (HEDP) experiments [42]. The fastest non-UXI cameras can capture images at 200 ns intervals, which is significantly slower than the dynamics of laser-shock compression on the order of a few nanoseconds. Here, with improved functionality, the Icarus V2 was deployed to record up to four XFEL pulses separated by 1-3 nanoseconds between each pulse, enabling us to directly visualize how material defects can contribute to the seeding and growth of hydrodynamic instabilities that evolve on the micron scale upon laser-driven shock compression (see Fig. 2.1). By combining UXI cameras with a train of high flux XFEL pulses (10^{12} photons/pulse) at the LCLS XFEL, potential 100 nm resolution images can be collected [31, 33, 40, 41, 43]. With the Icarus V2, we analyzed materials in the high pressure regime (several Mbar) and collected a series of up to four dynamic images separated by only a few nanoseconds that can provide novel insight on the formation and growth of instabilities in ICF materials [44]. In this work, we present the first application of multi-frame imaging from a XFEL pulse train to the Icarus UXI detectors.

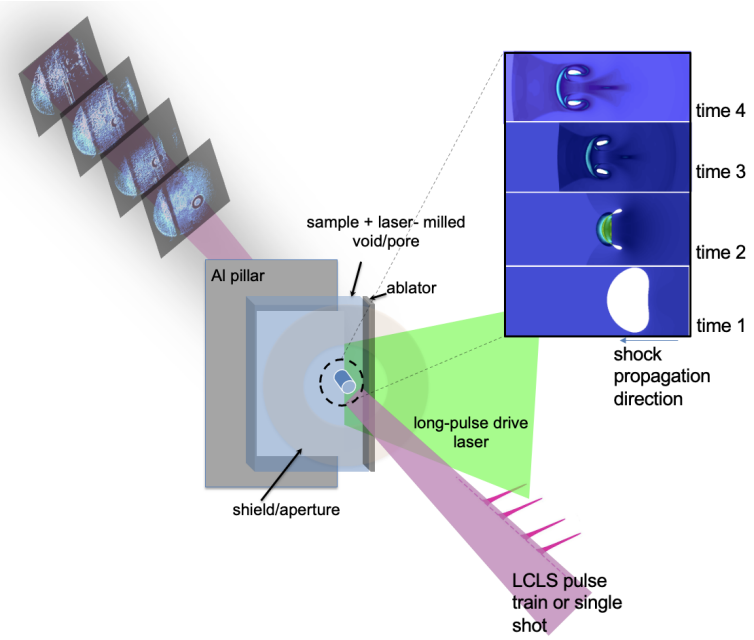

Figure 2.1 A schematic describing the experimental setup at the LCLS-MEC showing a four-pulse train illuminating a laser shock driven void in an SU-8 sample, generating a series of four x-ray phase-contrast images captured on the Icarus V2 camera. The upper right of the figure gives an example of changes in the void geometry. (Upper right inset adapted from ALE3D simulation [45], LLNL.)

2.2 Detector Description

Sandia and Lawrence Livermore National Laboratories developed the UXI sensors that were used in our experiments [42,46–49]. For our experiment, we implemented the Icarus V2 detector, which was housed in a 3D printed box. Triggering, data collection, and basic corrections, such as subtracting pedestals calculated from dark runs, were performed using standard LCLS tools [50]. The DAQ and camera timing setup were as described in Hart et al. [33]

The Icarus V2 sensor is a 1024 x 512 pixel, 4-frame burst-mode hybrid-CMOS sensor with 25 μm pixel pitch. It generates 4 unique and independently programmable shutters from an external

asynchronous trigger and distributes these shutters on a row wise manner. The array is split timing wise into East and West hemispheres to allow for 2 independently timed arrays of 1024 x 256 pixels [33, 42, 49]. The detector operated in the 1-2 timing mode where there is a 1 ns gate followed by a 2 ns reset. In a previous experiment at LCLS, the Icarus V1 was implemented to record wide-angle diffraction signal from two XFEL pulses separated by 4.2 ns for an x-ray pump x-ray probe experiment to measure ultrafast x-ray heating in copper [33]. This experiment and others demonstrated the effectiveness and capability of UXI cameras in recording multi-frame material dynamics [26, 31, 43].

The Icarus V2 camera is part of the UXI sensor family and is a multi-frame hybridized complementary metal oxide semiconductor (CMOS) sensor [42]. It is "hybridized" because a custom readout integrated circuit (ROIC) is bonded to an array of silicon photodiodes, which are 25 μm in pitch and is sensitive to soft and hard x-rays [49]. The Icarus V2 can capture images on the nanosecond time scale utilizing MOSFET switches as electronic shutters [42]. These shutters remove readout speed limitations by storing these frames in-situ on in-pixel storage elements and then reading off the stored charge on a slower timescale [47]. The shutters, also known as the "gate" in the context of UXIs, controls the pixel's integration time and gain [49].

This type of camera can collect data at the speeds required for ultra-fast timescale experiments. The collection speed is dictated by how many memory elements can fit into a given pixel [47]. Essentially, each pixel has a buffer that acts as temporary storage for the intensity measured by that pixel. The transfer of charge from the pixel to this buffer and clearing the pixel is fast enough to record data within 1 ns [47]. The use of a UXI camera was crucial for the success of the in-situ

experiments presented here.

2.3 Experimental Details

To study the shock-void wave interactions, we imaged the evolution of micro-voids within the sample with multiframe x-ray phase contrast imaging. We used a train of four x-ray pulses with pulse widths between 40-80 fs at 8.23 keV to observe micro-void compression in low density polymers at the sub-micron length scale (see Fig.2.1). For the first time, with the Icarus V2, we acquired a series of four x-ray phase-contrast images (XPCI) at the LCLS.

At the MEC instrument we used the 60 J, Nd:glass laser system to provide long-pulse laser ablation to shock our samples [40, 41]. This system operates at 1054 nm and the pulse is split into two arms to eventually become frequency-doubled to 527nm [40,41]. The pulse-shaping capabilities at MEC allow users to produce laser pulses with duration ranging between 2 and 200 ns. [40, 41]. For two experimental runs (runs 292 and 295), we used a 10 ns quasi flat-top optical pulse. The laser was focused down to a 300 μm spot on the sample.

Figure 2.2 shows the temporal profile of the laser drive pulse that was used in our experiment. The main drive pulse was set to have a quasi-flat top square profile of 10 ns duration. The pulse profile recorded by the oscilloscope (Fig. 2.2) shows a temporal modulation that deviates from an ideal flat top shape. This effect has been mitigated later during the experiment by acting on the pulse slicer (Pockels cell). Furthermore, an additional low-intensity pulse was detected, as shown in the inset in Fig. 2.2. The presence of two distinct features in the driver profile, i.e., a low-intensity

pre-pulse preceding the main laser pulse, results in a double-stage compression. An initial shock at moderate pressure is launched through the sample, followed by the main compression shock wave. The signature of both the low- and high-pressure shock have been identified in the PCI images, as discussed in the following section.

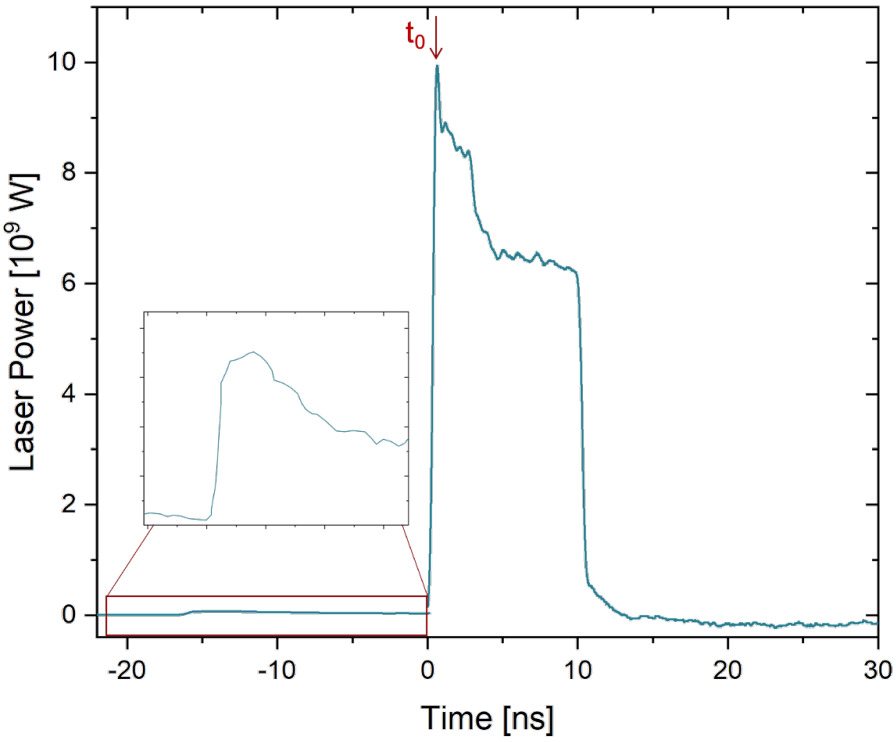

Figure 2.2 Oscilloscope trace of the shape of the optical laser shock drive profile for run 246. The inset plot shows the shape of the pre-pulse (1J), i.e., a low-intensity laser pulse that drives compression at moderate pressure prior to the main flat top drive pulse. t0 is the start of the main compressive wave on the sample.

The XFEL four-pulse train at LCLS provides four bursts of x-ray pulses [51], which enabled us to image in-situ, the changes in the sample's structure on the UXI camera. The pulses have adjustable time separation (see Fig. 2.3) and captured the x-ray phase-contrast images of the sample in real time during shock compression. While four frames were recorded with the UXI, the third

frame had consistently low signal either due to low x-ray pulse intensity or fluctuating timing, and therefore it is not shown here.

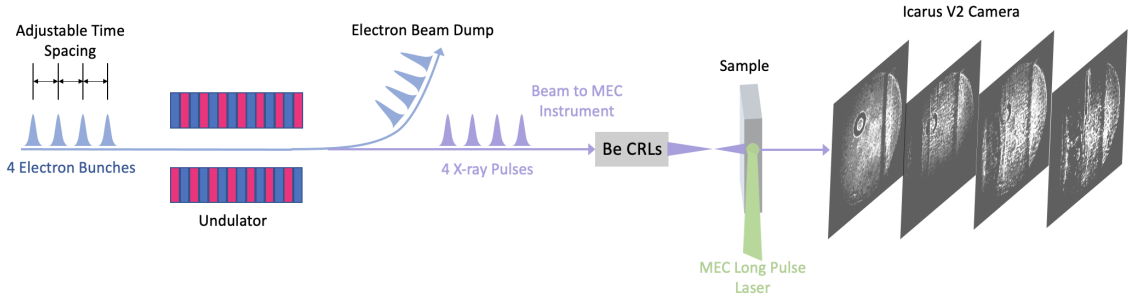

Figure 2.3 A schematic describing the XPCI setup and the pulse separation the the XFEL four-pulse train at LCLS. (Figure adapted from Hart et al. [33])

The highly coherent XFEL beam and the Icarus V2 detector enabled time-resolved phase-contrast imaging with high spatial resolution. To obtain high resolution images, we used 40 Beryllium compound refractive lenses (50 μm radius of curvature and 300 μm aperture) to focus the XFEL pulses to a 150 nm spot FWHM 197 mm behind the optics, which expands to 275 μm at the photoresist SU-8 samples 158 mm behind the focus. We calibrated the spot size using a 12.5 μm pitch nickel grid.

Since a single target is destroyed within microseconds for each laser shock drive, we loaded several samples on cartridges at a time. The setup included a motorized stage with six degrees of freedom, which gave an area of 150 mm x 25 mm to mount targets. We stationed the Icarus V2 detector 4.583 meters after the samples at the end of a long flight tube connected to the samples and capped with a polyimide window. The effective magnification of the setup is 29 giving us an effective pixel size of 850 nm, much larger than the potential resolution of 150 nm from the nanofocused spot. This resolution is pixel- size and geometry-limited in our experimental configuration due to

the larger field of view desired (275 μm) on the sample.

2.4 Data Analysis

At the MEC instrument, we recorded multiple runs with the Icarus V2 camera. However, during the alignment of the system some pixels on one half of the detector were exposed to unattenuated light, damaging part of the detecting area (possibly caused by a spurious reflection of the shock laser drive or XFEL beam being unattenuated). These damaged image areas can be seen in run 292 involving this fast-framing detector. An example of the inpainting algorithm is illustrated in Fig. 2.4 using a static frame from run 292. We applied this algorithm to three additional frames for run 292 and refer these inpainted images from here on out. To fill the damaged areas in the images, both the texture and the geometry of the images were considered. Through the use of the built-in exemplar-based inpainting algorithm in MATLAB, we were able to fill in dead pixels by simultaneously propagating textures and geometry. Fig. 2.4 demonstrates the efficiency of the inpainting algorithm that has been applied to the images presented in the following (Fig. 2.5). This algorithm is based on the work of Criminisi et al. [52]. The benefit of using this algorithm is that it does not suffer from blurring via diffusion processes in large damaged regions.

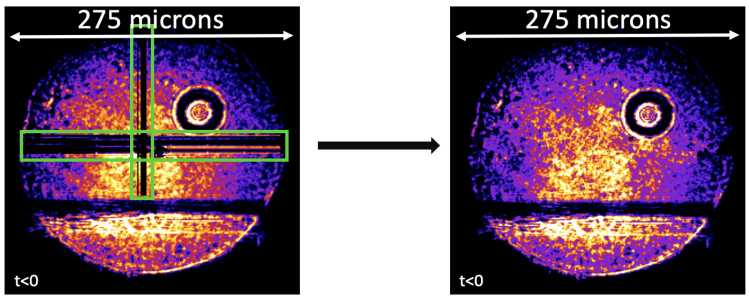

Figure 2.4 Example of inpainting of damaged pixels in run 292 where we captured a series of x-ray phase-contrast images with the Icarus V2 fast-framing detector. The left image represents a real image we recorded on the Icarus V2 with damaged rows and columns shown with green boxes. The right image displays the results of exemplar-based inpainting [52].

The exemplar-based algorithm begins by a user locating a specific region to be fixed or filled. This is the "target" region, while everything else in the image is the "source" region. The priority of filling in this algorithm is based on a confidence and data term, which helps determine the priority of the patch to be filled in the "target" region. The patch with the highest priority in the "target" region is chosen to be filled from the most similar patch in the "source" region. This best patch is found by the sum of square differences (SSD). Simultaneously, the data term propagates geometry and the confidence term propagates textures into that "target" region. There is a trade-off between the confidence and data terms, such that the linear structures or geometry is synthesized first before textures fill in the dead pixels. The confidence value is updated and the process repeats until the "target" region is entirely filled.

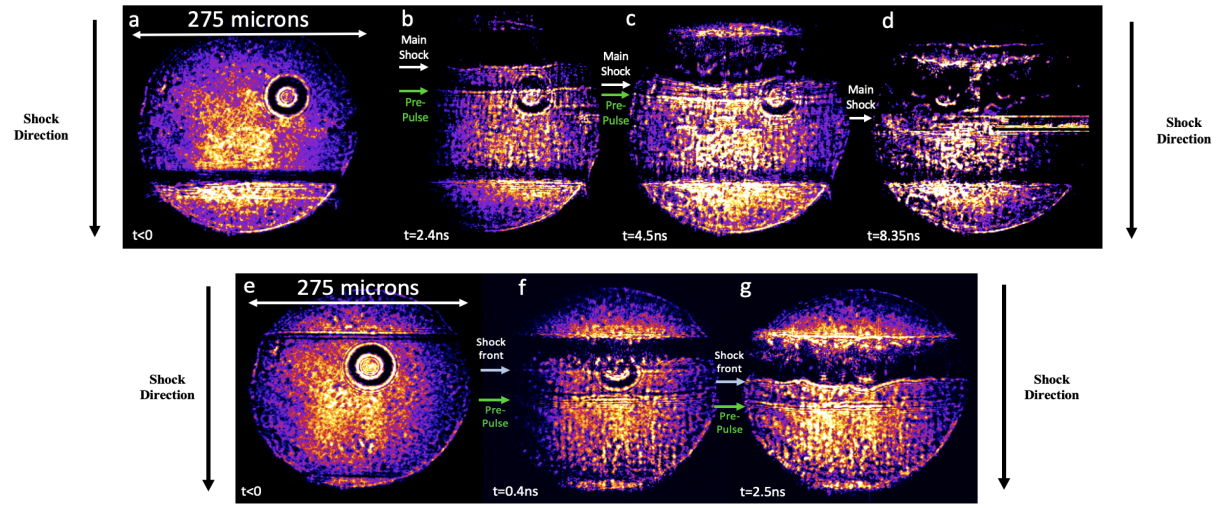

Figure 2.5 (a-d) X-ray phase-contrast images for run 292. A 10 ns flat-top pulse was used to drive a shock wave into the SU-8 sample. The t<0 frame is the static pre-drive image. The XFEL beam spot diameter at the sample position is 275 μm. Three frames of the four-pulse train x-ray phase-contrast images are shown from LCLS at 8.23 keV of a SU-8 photoresist sample during passage of a laser-driven shockwave. Relative timing is shown in the lower corner of each frame. A weak shock from the pre-pulse, indicated by a green arrow, travels downward at a speed of 2.95+/-0.3 km/s, resulting in a pressure of $\sim$1.4+/-0.6 GPa. The pre-pulse is followed by the main pulse that travels at a speed of 9.44+/-0.6 km/s, resulting in a pressure of $\sim$50+/-9 GPa. (e-f) X-ray phase-contrast images for run 295. A static pre-shot (t<0) and two dynamic images from the four pulse train were collected. The pre-pulse travels as a speed of 3.54+/-0.3 km/s, resulting in a pressure of $\sim$2.7+/-0.8 GPa. The main pulse travels at a speed of 10.62+/-1.0 km/s, resulting in a pressure of $\sim$71+/-19 GPa.

As shown in Fig. 2.5, we can see that the Icarus V2 is capable of capturing multiple frames from a single sample as it is laser shocked on the few nanosecond time scale. We note that the Icarus V2 camera was able to record and readout four frames, but low x-ray pulse intensity or fluctuating timing caused one frame in run 292 and two frames in run 295 to have very low signal. As a result, those frames are not included.

As can be seen with images (a-d) in Fig. 2.5, we retrieved four x-ray phase-contrast images of

a SU-8 sample, a low-density polymer, with a 40 μm hollow glass void and we can observe the changes taking place in the sample upon passage of a shock wave on the nanosecond scale. In frame (a) in Fig. 2.5, we have a static image, where we can clearly see a micro-void. Then, 2.4 ns later in frame (b) in Fig. 2.5, we can see two shock waves: first a weak elastic shock propagating through the material (indicated by a green arrow), maintaining its planar shape as it passes through the void; it is also worth noting that the void geometry is not altered after interaction with this first compressive wave. After 4.5 ns (frame c in Fig. 2.5) since the initial XFEL pulse, the second shock front (indicated by a white arrow), i.e., the one caused by the main flat top pulse (see Fig. 2.2), interacts with the void altering the material structure. This high pressure wave induces strong changes in material density and a dark band surrounding the shock front is visible in the data.

As seen from (e-g) in Fig. 2.5, the Icarus V2 camera captured three frames of another SU-8 photoresist sample. In this run, we were able to only collect two dynamic frames since we had low signal due to low x-ray pulse intensity or fluctuating timing. In the first frame, we have a static image with a glass micro-void. Then 0.4 ns after the initial pulse (frame f in Fig. 2.5), we can see both the low- and the main high-pressure waves (indicated by green and white arrows). At 2.5 ns (frame g in Fig. 2.5), the distance between the low- and the high-pressure wave front has diminished, confirming that the second wave travels at a higher speed. From frame (g) in Fig. 2.5, we can also appreciate the changes in the shock front profile, that does not appear planar most likely because of the interaction with the void. This uneven compression could give rise to hydrodynamic instabilities, laser boring, ablation layer nonuniformities, etc.

In these runs, the shock velocity (Us) for both the low- and high-pressure shock waves has been

estimated by analyzing the motion of the shock front in successive frames acquired from a single sample. The equation of state of polyimide, a polymer analogue to the SU-8 photoresist and of comparable density (1.146g/cm^3) was used to infer the pressure state reached along the Hugoniot curve upon shock compression [53]. For run 292, the pre-pulse generates a weak elastic shock wave that propagates through the sample with a shock speed of 2.95+/-0.3 km/s, corresponding to a pressure around 1.4+/-0.6 GPa; the main pulse generates a higher pressure state, i.e., 50+/-9 GPa, with an estimated shock speed of 9.44+/-0.6 km/s. Similarly, for run 295, the pre-pulse generates a weak elastic shock wave that propagates through the sample with a shock speed of 3.54+/-0.3 km/s, corresponding to a pressure around 2.7+/-0.8 GPa; the main pulse generates a higher pressure state, i.e., 71+/-19 GPa, with an estimated shock speed of 10.62+/-1.0 km/s. From these runs we see that the pre-pulse generated a low-energy elastic shock wave, compressing the sample to an initial pressure of a few ($\sim$1-3) GPa, while the main pulse produced higher pressure shock states up to $\sim$50-70 GPa. Despite having the same nominal pulse profile, the shot-to-shot variation and the presence of the pre-pulse made it difficult to reproduce consistently the same pressure conditions in the samples over different runs.

The turbulent appearance of the dark band is due to the occurrence of the laser-plasma instabilities and other hydrodynamic instabilities in the shock front. The origin of the dark band visible in the data could be, as suggested by PCI simulation (see Fig. 2.6), the refraction and diffraction phenomena taking place at the shock front. Mitigation of this dark band can be achieved with higher x-ray photon energies, which is shown in Fig. 2.7. Additionally, there are small fragments that appear in the dark band after the optical pulse propagates through part of the material. These fragment

structures in the dark band could be explained by laser boring into the sample or imperfections in the ablation layer.

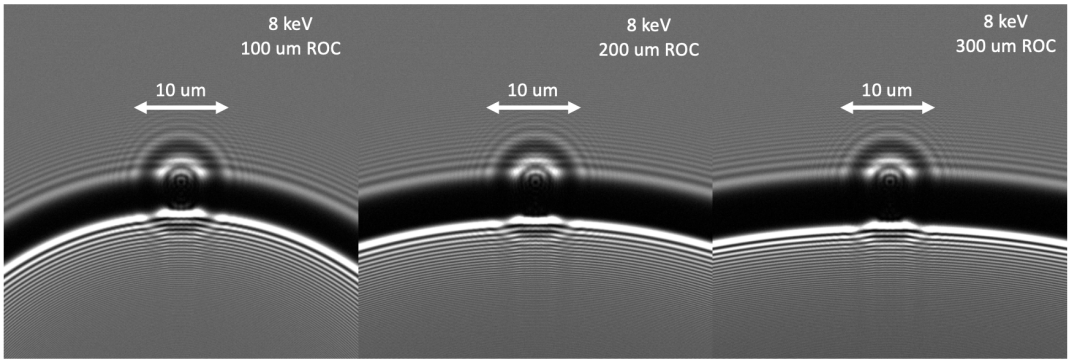

Figure 2.6 This simulation describes different radius of curvatures (ROCs) of the shock front for 8 keV x-rays and its impact on void collapse.

The curvature of the shock front, the density jump between shocked and unshocked material, the size of the void, and the x-ray probe wavelength are all contributing factors that affect our ability to image the void as a shock or compressive wave propagates through it. To better interpret the experimental data, we performed phase-contrast imaging simulations of synthetic phantom objects to reproduce our experimental geometry. A density jump with varying radius of curvature interacting with a spherical void was used to mock up the shock front for compression at varying pressures, as shown in Fig. 2.6. Increasing the simulated "shock" radius of curvature increases the phase jump, increasing the dark band width due to refraction. These same phantom phase-contrast simulations, depicted in Fig. 2.7 also indicate that using higher x-ray photon energies will reduce the width and darkness of the band, allowing better visibility of the void during shock passage.

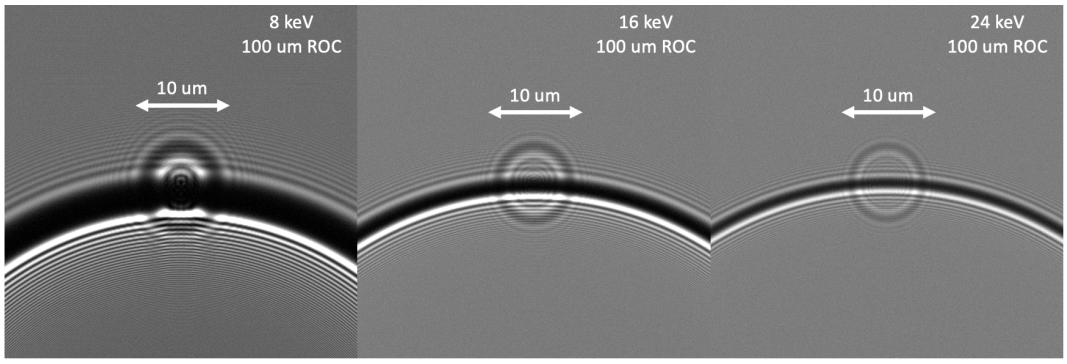

Figure 2.7 A simulation that demonstrates that with increasing x-ray photon energy, the dark band width is reduced in size. This enables better visibility of the void undergoing shock compression. In this example, the same radius of curvature (ROC) for the shock wave is used.

2.5 Conclusions

Here, we used the XFEL four-pulse train at LCLS to image dynamically changing materials under laser shock compression at the MEC instrument for the first time, allowing us to make preliminary but substantive comparisons with simulations of void collapse. With the unique high flux and brilliance from the XFEL, we obtained multi-frame x-ray phase-contrast images with high spatial and temporal resolution captured by the Icarus V2 fast-framing camera. The Icarus V2 camera is beneficial to XFEL science as it is primed for burst mode data collection and compatible with the time frames for dynamic compression, on the order of a few nanoseconds [42]. Examining the effect of material heterogeneities, like micro-voids, on material properties during the passage of a laser-driven shock wave is important for benchmarking the performances of ICF energy materials at extreme conditions. Our novel method for in-situ ultrafast imaging will allow characterization

of void response to laser shock compression will and provide fundamental insight on how to minimize the growth of instabilities that occur at the micro scale. Now it will be possible to develop better predictive models and improve materials design with information gathered from materials dynamically changing in extreme conditions.

LCLS has the capability of producing x-ray pulses with a temporal spacing as short as 350 ps [31, 43]. We anticipate using new hard x-ray sensor UXI detectors currently in production in future runs to study void-shock interactions at the sub-nanosecond time scale. This will allow imaging of processes that evolve at an even faster timescales with high resolution, providing novel insights on how the voids size affects void collapse, collapse rates, jetting formation, interaction with the shock front, formation of hot spots, and plasma properties. This will enable us to see through the dark band that was previously mentioned and will give information on microstructural features that appear in the void collapse process.

Chapter 3

UXI results in the direct-imaging regime

Below is the text from a submitted manuscript to the Optics Express Ultrafast Optical Imaging Feature Issue titled, **"Multi-frame, ultrafast, x-ray microscope for imaging shockwave dynamics"** by D. S. Hodge, A. F. T. Leong, S. Pandolfi, K. Kurzer-Ogul, D. S. Montgomery, H. Aluie, C. Bolme, T. Carver, E. Cunningham, C. B. Curry, M. Dayton, F. J. Decker, E. Galtier, P. Hart, D. Khaghani, H. J. Lee, K. Li, Y. Liu, K. Ramos, J. Shang, S. Vetter, B. Nagler, R. L. Sandberg, A. E. Gleason [54]

Abstract. Inertial confinement fusion (ICF) holds increasing promise as a potential source of abundant, clean energy, but has been impeded by defects such as micro-voids in the ablator layer of the fuel capsules. It is critical to understand how these micro-voids interact with the laser-driven shock waves that compress the fuel pellet. At the Matter in Extreme Conditions (MEC) instrument at the Linac Coherent Light Source (LCLS), we utilized an x-ray pulse train with ns separation, an x-ray microscope, and an ultrafast x-ray imaging (UXI) detector to image shock wave interactions with micro-voids. To minimize the high- and low-frequency variations of the captured images, we incorporated principal component analysis (PCA) and image alignment for flat-field correction. After applying these techniques we generated phase and attenuation maps from a 2D hydrodynamic radiation code (xRAGE), which were used to simulate XPCI images that we qualitatively compare with experimental images, providing a one-to-one comparison for benchmarking material performance. Moreover, we implement a transport-of-intensity (TIE) based method to obtain the average projected mass density (areal density) of our experimental images, yielding insight into how defect-bearing ablator materials alter microstructural feature evolution, material compression, and shock wave propagation on ICF-relevant time scales.

3.1 Introduction

In inertial confinement fusion (ICF) experiments, such as the recent 1.3 MJ record shot at the National Ignition Facility (NIF) [22], high-energy lasers were converted to x-rays via a hohlraum and were used to compress a fuel capsule. These laser beams ablated the capsule's external layer, which turns into a plasma and quickly compresses the fusion fuel to extreme pressures via shock waves. Analyzing the physical and chemical modifications in ablator materials containing voids at extreme conditions on the micron and nanosecond scales is crucial for advancing ICF, inertial fusion energy (IFE) research and theoretical models [10, 55–57]. Multiple experiments have indicated that yield degradation arises by growth of hydrodynamic instabilities, such as the Rayleigh-Taylor and Richtmeyer-Meshkov instabilities, at the fuel-ablator interface [3, 4, 19, 58–60]. Specifically, experiments conducted at the NIF, have suggested that one of the main causes of these instabilities are micro-voids in the ablator, which induce a jet of material from the ablator surface, negatively influencing the capsule's performance and prevent attainment of the pressures and densities required to initiate thermonuclear ignition [8, 61]. Therefore, to understand how voids contribute to the seeding and growth of hydrodynamic instabilities, we dynamically image void-shock interactions at the nanosecond timescale at 9 keV in a direct-imaging geometry (see Section 3.2).

Our experiment utilized a high-intensity laser to compress a hollow silica shell void embedded in SU-8 photoresist [34]. To capture the evolution of the shock front as it propagates through a sample, we combined the x-ray free electron laser (XFEL) four-pulse mode at the LCLS and the Icarus V2, an UXI camera, to obtain four frames of a single sample undergoing ablation-driven shock-compression. These images are captured over an 8 ns time frame [33, 42, 46, 47, 62, 63], a unique capability

that has the potential to revolutionize dynamic imaging for high-energy density physics (HEDP) experiments and other experiments studying ultrafast phenomena [33]. Previous experiments only had the capability of capturing one or two dynamic frames, which limited the analysis of sample evolution [40, 48, 64–67]; with the Icarus V2 detector, images are collected in sequence with greater temporal fidelity, providing a complete picture of the sample's dynamic evolution. In this work, we demonstrated the capabilities of this experimental approach in characterizing void-shock interaction in extreme conditions. Our data provides a movie displaying distinctive features arising from a void-shock interaction and compression with 700 nm spatial resolution.

Flat-field correction (FFC) is performed to normalize against spatial variations in the x-ray beam profile and artifacts accumulated along the x-ray beam. This is important in improving visualization of features in the sample, but also for extracting quantitative areal density information. To account for the stochastic nature of the XFEL beam we developed a FFC approach combining PCA [68] and image alignment [69, 70]. The former accounts for variations in the x-ray pulse intensity profile and normalizes against it, while the latter accounts for motion of artifacts induced by the varying x-ray pulse energy. We applied our FFC technique to single XFEL pulse images of shock-compressed micro-voids and visually compare these images with its simulated counterpart using phase and attenuation maps generated from a 2D radiation hydrodynamic code (xRAGE). Finally, we employed a TIE based approach to recover the mass density averaged along the x-ray direction (i.e. areal density). In the remainder of this paper, this will be referred to as the "average mass density map" (areal density) of the sample as it is compressed [71, 72]. The comparison between simulations and measured mass density advances our understanding of seeding and growth of hydrodynamic

instabilities caused by micro-void compression initiated by a laser-driven shockwave.

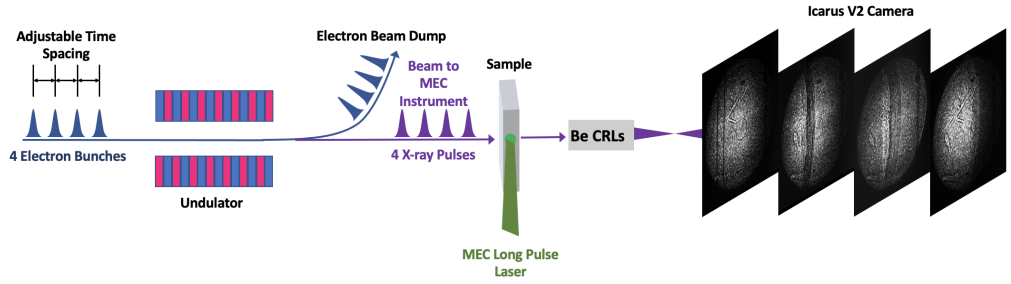

Figure 3.1 A schematic describing the direct-imaging setup and the pulse separation for the XFEL four-pulse train at LCLS. Four pulses are sent in at the same time as a laser shockwave interacts with our sample. The Icarus V2, an ultrafast x-ray imaging camera, captures four frames of this single sample during compression.

This paper is organized as follows: In Section 3.2 we briefly discuss the experimental design using a high-intensity long-pulse laser to shock-compress a sample containing a void. Then, we describe the UXI camera and its capability in capturing void-shock dynamics with high temporal resolution. In Section 3.3, we discuss the challenges of imaging void-bearing samples in the holographic regime and discuss the limit of different configurations in visuality of features behind the shock front. We introduce a direct-imaging approach which can improve visualization of void collapse and simplify extraction of mass density compared to the holographic regime. In Section 3.4, we introduce our FFC algorithm to reduce random fluctuations from the XFEL pulses and lens defects in our images. We compare our FFC images to simulated XPCI images to gain qualitative understanding of void-shock interactions and instability growth. Finally, we show our retrieved mass distribution between successive frames as a shockwave propagates through a void, yielding insight into void-shock interaction. The primary purpose of this work is to demonstrate a novel experimental platform to capture multiple *in situ* images of a single sample over nanosecond

timescales. This technique can be applied to the study of micro-void collapse upon laser-driven shock-compression, which understanding is key to advancing ICF science, as well as other ultrafast phenomena.

3.2 Experimental setup for direct x-ray imaging

In this proof of principle experiment, we used SU-8 photoresist and hollow silica microspheres as proxy for the ablator material and the voids, respectively. SU-8 [73] was an ideal choice since it has similar properties and shock response to traditional ICF ablators and provides a homogeneous layer and lateral wall quality essential for uniform shock propagation and dynamic x-ray imaging. Hollow silica microspheres were used as proxy for voids and provide several advantages such as their size reproducibility, cost reduction, and time saved compared to other fabrication methods. Additional information about the selected materials and the fabrication techniques used for this experiment and its impact on future HEDP experiments is detailed by Pandolfi et al. [34].

Prior to the experiment, accurate tuning of the fabrication procedure enabled precise and consistent placement of the voids within the material for our desired experimental geometry. Fig. 3.1 shows a schematic view of our experimental setup, which are detailed in the following section.

3.2.1 High-intensity long-pulse laser for shock compression

Delivery of a laser shockwave to our samples required the 60J, Nd:glass laser system located at the MEC at LCLS [40, 64]. This laser provided high-energy pulses at 527 nm [40] with a 10 ns

flat-top profile. High energy pulses were delivered as the summed contribution of four separate arms, depicted in Fig. 3.2a. The intensity of the pulses varied up to 5% between dynamic shots, but feedback diagnostics were implemented to correct pulse variability.

The drive laser was used to compress a 42 micron diameter hollow silica shell (2.65 g/cm^3 as given by Cospheric LLC, USA) embedded within SU-8 photoresist material (1.2 g/cm^3 [74]). The four laser amplifier arms were focused down to a 150 μm spot size, delivering a pulse energy of 76.2 J to the sample. The temporal profile for this dynamic run is shown in Fig. 3.2a. Figs. 3.2b and 2c display our beam geometry and the dimensions of our sample (2.5 mm x $\sim$150-160 μm x 400 μm) as viewed along different beam paths, which are perpendicular to each other. These sample dimensions were designed such that edge effects were not an important factor during void-shock compression. Fig. 3.2b shows a 25 μm thick Kapton layer and 300 nm aluminum layer that were added to the sample to act as ablator and heat-shield, respectively, and to provide a reflective layer for the velocimetry diagnostic. An electro-optic modulator temporally manipulated the laser pulses to generate the ideal flat-top shape, reducing inhomogeneous energy delivery to our samples.

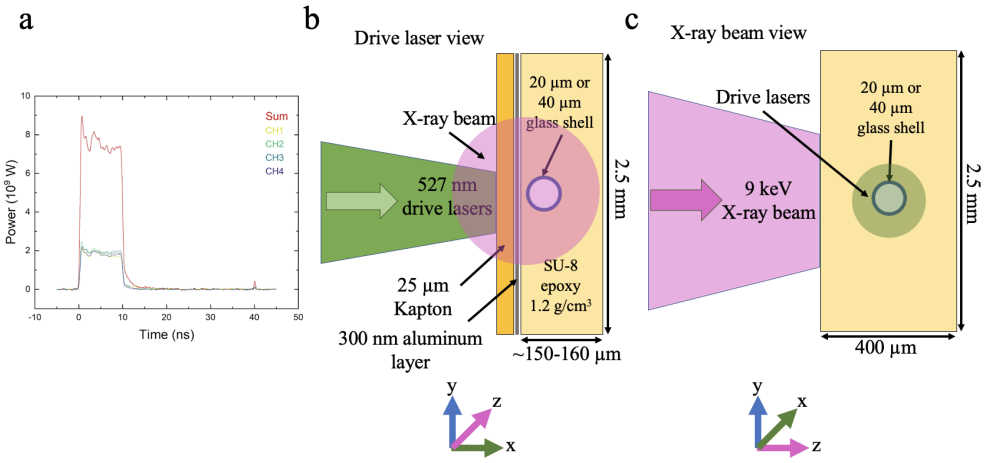

Figure 3.2 **Panel (a)** is the oscilloscope trace of the void-shock dynamic run for the X493 experimental campaign. The energy delivered to the sample by each arm (denoted by colors yellow, green, blue, and purple) is nearly identical, summed to give us the red solid line, a 10 ns flat-top pulse. **Panel (b)** displays our target schematic of fabricated void samples with laser drive orientation. The corresponding dimensions are given for the different layers. Additionally, the dimensions for the SU-8 sample is given (height of 2.5 mm and ∼150-160 μm thick along the drive laser path). **Panel (c)** shows a rotated view of panel (b), displaying the dimension of the sample along the z-direction (400 μm thick along the x-ray propagation direction). Colored axes are given below each target schematic to indicate the drive (green) and x-ray (purple) path directions. The x-ray probe is perpendicular to the shock propagation direction. **Note**: The schematics drawn in panels (b) and (c) are not drawn to scale, but are meant to give a general understanding of our experimental geometry.

By collecting multiple frames from a single shock-compressed sample, we could directly visualize the propagation of the shock front through the sample. Since the time interval between each frame is fixed by the XFEL four-pulses temporal profile and the images were spatially calibrated, it was possible to directly measure Us, i.e., the shock-wave velocity for each consecutive frame. Using the measured values for Us and the polyimide equation of state [75], we could infer the pressure attained during shock compression, as well as monitor eventual acceleration or decelerations in the shock-wave propagation due to interference with the void.

3.2.2 XFEL nanosecond pulse train imaging

In the XFEL multi-pulse mode, we illuminated our samples with a series of four pulses with pulse widths of 40-80 fs and pulse separation of ∼2-4 ns to create a movie of micro-void compression at the micron length scale (see the bottom row of Fig. 3.3). The XFEL spot size on target was 300 μm, providing a large field of view to visualize the shock front as it propagated through the void. We calibrated this spot size by using a copper 2000 mesh TEM grid. An x-ray microscope was employed to image in the direct-imaging regime, which comprised of 52 beryllium compound refractive lenses (CRLs) (50 μm radius of curvature and 300 μm aperture) placed 130 mm downstream of the sample. This enabled a magnification of 40X and an effective pixel size of 700 nm. These parameters remained the same for the duration of this experiment. We analyzed how the material structure is altered at and around the micro-void location and how the structure behaves during compression. This setup was previously demonstrated in PCI geometry with the lenses upstream of the sample [35].

3.2.3 Icarus V2 - ultrafast x-ray imager

A critical element that is required for nanosecond imaging is the Icarus V2, an ultrafast x-ray imaging camera. We stationed the Icarus V2 detector 4.3 m downstream of the sample at the end of a vacuum flight tube to capture four magnified images of a single sample during laser shock compression. Although four frames were recorded, the last frame was not considered in our dynamic runs since it had consistently low x-ray intensity. This resulted in a low signal-to-noise-ratio that prevented analysis of the data. Therefore, we only include the first three frames captured on the

UXI camera, which are presented together with the static frame acquired before the compression occurs (see Fig. 3.3).

LCLS's capability of delivering several ultrashort, highly coherent x-ray pulses has enabled simultaneous high spatial and temporal resolution that was previously unachievable [25, 27, 28, 31–33, 35, 76]. The accelerator at LCLS has the potential of delivering a pulse train up to 8 bunches with a minimum bunch separation of 350 ps [33]. With the advent of the UXI camera these pulse structures can be exploited to capture up to four images separated by $\sim$2-4 ns, paving the way to understanding material dynamics in extreme states at the micron and nanosecond scale.

Sandia National Laboratories (SNL) developed the Icarus V2 for the study of HEDP experiments that occur on ultrafast time scales [33, 42, 46, 47, 62, 63]. The Icarus V2 is a burst mode style imager that is 1024x512 pixels with 25 μm pixel pitch [33,46,47,62]. This fast-gated hybrid complimentary metal oxide semiconductor (hCMOS) detector can simultaneously provide multiframe 2D images and temporal information on nanosecond time scales, comparable to the time evolution needed in ICF experiments [46, 47, 62]. hCMOS imagers overcome many of the existing limitations in previous imagers [46, 47], providing a wider dynamic range and on-device storage of 4 frames per pixel, over 0.5 million pixels, a full well capacity of 600k electrons for each pixel, sensitivity to both soft and hard x-rays, and gate times of $\sim$1.5 ns [46, 47, 62].

The Icarus V2 has adjustable timing modes available and the exposure time is defined by the readout integrated circuit (ROIC), which is described in detail by Hart et al. and Claus et al. [33, 46, 47]. One constraint for this camera is that a minimum integration time per frame of 2 ns is required. For this experiment we ran the Icarus V2 in the 1-2 timing mode with an effective

signal integration time of 700 ps every 3 ns. This enabled us to capture $\sim$ns snapshot images of void-shock evolution. More information about the timing modes for the UXI detector is described by Hart et al. [33]. For this experimental campaign the time separation between pulses captured by the UXI was 2.1 ns, 3.85 ns, 2.1 ns. To avoid readout speed limitations, metal-oxide-semiconductor field-effect transistor (MOSFET) switches are used as electronic shutters or gates, which controls the pixel integration time and gain [33,46,47]. These frames are stored on in-pixel storage elements and the images are read off on a slower time scale [33,46,47]. For our readout system we incorporated readout hardware and software from Lawrence Livermore National Laboratory (LLNL) into the LCLS Data Acquisition System (DAQ). Additionally, standard LCLS tools [50] were used for initial image correction (i.e. image geometry alignment and background subtraction). The capabilities of the UXI camera are illustrated in Fig. 3.3b-d, where we visualize the shock propagating through a hollow SiO_2 void embedded in SU-8.

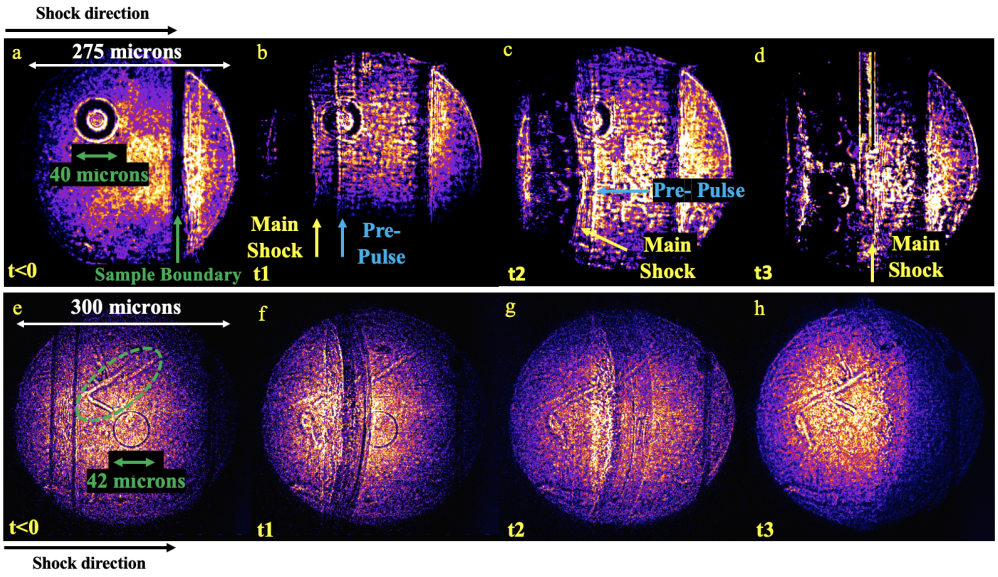

Figure 3.3 Each row shows data acquired from a single sample during shock-compression using two different imaging setups and techniques. **Top row(a-d)**: LV08 experimental campaign at LCLS. Four x-ray phase contrast images (holographic regime with XFEL energy at 8.23 keV) of a hollow 40 μm diameter void embedded in SU-8 material undergoing laser shock compression collected using the Icarus V2 [35]. A 10 ns flat-top shock wave was delivered to this sample, which is indicated by a yellow arrow in frames b, c, and d. Behind the shock front (left to the yellow arrow) is a dark band, i.e. features that cannot be imaged in this geometry due to strong refraction effects due to the phase-contrast imaging geometry and lower photon energy. **Bottom row(e-h)**: X493 experimental campaign at LCLS. Four x-ray images acquired in direct-imaging configuration (XFEL energy at 9 keV), showing a 42 μm diameter void in SU-8 material undergoing laser shock compression. A 10 ns flat-top pulse was delivered to this sample and the void-shock interaction is easily visible compared to the images displayed in the top row. The green dashed line encircles a Be lens blemish in frame e that is not part of the sample.

3.3 Results: Comparison of XPCI imaging in the holographic and direct-imaging regime under shock compression

Propagation-based x-ray phase-contrast imaging (XPCI) uses quasi-coherent x-rays to illuminate a sample while a detector is placed a sufficient distance away to record Fresnel fringes formed by interference between scattered and unscattered x-rays [24, 77, 78]. Compared to conventional radiography, this imaging modality enhances the contrast of weakly absorbing objects, such as the shock front and void. Furthermore, compared to other XPCI imaging modalities such as analyzer-based XPCI and x-ray interferometry [79, 80], it can use all of the available photons for illumination. These properties are particularly advantageous for photon-starved regimes, such as in ultrafast x-ray imaging. When performing propagation-based XPCI, an important parameter to consider is the Fresnel number

$$\mathrm{Fr} = \frac{a^2}{\lambda L}, \tag{3.1}$$

where a is the size of the object illuminated, λ is the wavelength, and L is the distance from the sample to the detector. This number dictates how much phase-contrast is introduced into the image. When Fr $\simeq$1, also known as the holographic regime, features in the image are significantly enhanced by phase-contrast. In our previous experiment we imaged at Fr $\simeq$1, operating at 8.23 keV and capturing a series of phase-contrast images of void-shockwave interaction by combining the four-pulse train at LCLS with laser shock compression. [35]. The XPCI data collected using the UXI camera (field of view (FOV) 275 μm) are displayed in the top row of Fig. 3.3. A laser

shockwave propagated through our sample with a Us of 10 km/s, resulting in a pressure of $\sim$50 GPa. This was the first demonstration at an XFEL where the Icarus V2 was implemented to capture multiple frames, giving insight into how voids affect shock front evolution and overall ablator performance [35].

However, Fig. 3.3 (top row) shows strong phase-contrast in the form of a dark band, visible in the regions behind the shock front, obstructing our view of the void-shock interaction. To verify the origin of the dark band, we compared our experimental data with simulated XPCI images [35], confirming that imaging at 8.23 keV in the holographic regime obscures the dense region behind and along the shock front [35]. To reduce the amount of phase contrast, we employed a direct-imaging geometry in another void-shock experiment at 8.28 keV and captured a single static and dynamic image of void-shock evolution using the Andor Zyla camera, a single frame detector with 6.5 μm pixel pitch. A collection of parameters for this experiment and the others are contained in Table 1 in the supplemental information. Switching to the direct imaging regime for this experiment involved moving the stack of Be CRLs (25 lenses) from upstream to downstream of the sample. The magnification was 20X for this particular experiment. This placement effectively reduced the sample-to-detector propagation distance and consequently increased $Fr>1$. This is also known as the near-field regime. Images captured in this regime are displayed in Fig. 3.4. The orange arrow included in Fig. 3.4b and Fig. 3.4c is included to denote the shock front. The phase-contrast effects are significantly reduced in this configuration in comparison to the images in the top row of Fig. 3.3, demonstrating the superiority of the direct-imaging configuration. Although the Andor Zyla camera provides a higher spatial resolution, it cannot capture the dynamics with the same

temporal fidelity as the UXI camera. Even though a single dynamic image can give significant insights into void collapse, this limitation to a single frame restricts our ability to fully grasp how void-shock interactions evolve on ICF-relevant time scales.

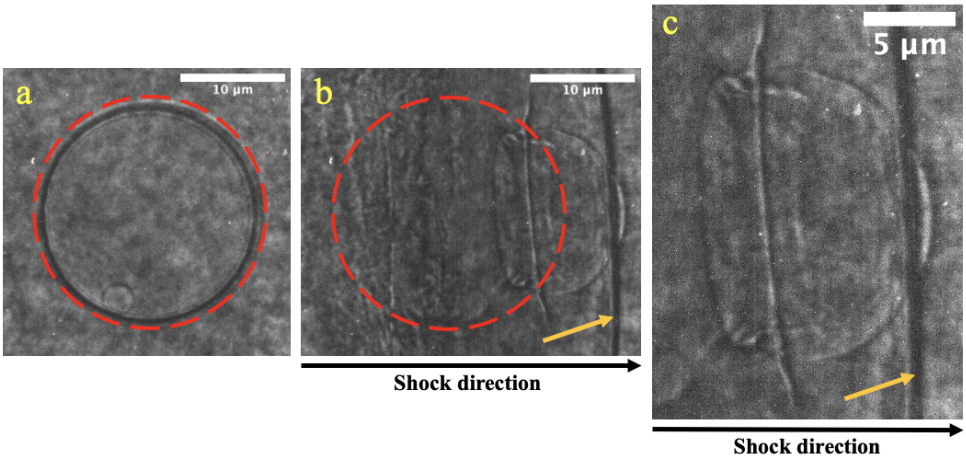

Figure 3.4 **Panel (a)**: Static image of a hollow void (SiO_2) that is 20 μm in diameter with a FOV of 100 μm. This void is embedded in SU-8 material. The red circle indicates the location of the void to track its displacement in panel (b). **Panel (b)**: Dynamic image where a high-intensity long-pulse laser compresses the void. The dashed red circle displays how much the void has shifted compared to the initial image in panel (a). The orange arrow points to the shock front after it has nearly propagated through the void. **Panel (c)**: Zoomed in image of the void from panel (b) for better visibility of the void features and shock front. For emphasis, the orange arrow points to the shock front. **Note**: These single frame static (panel (a)) and dynamic images (panel (b)) were acquired in the X437 experimental campaign. They were captured with a single frame detector, the Andor Zyla, which has a higher pixel pitch (6.5 μm) as compared to the faster UXI camera with 25 μm pixel pitch.

In our current experimental campaign we adopted this direct imaging configuration and combined it with the UXI camera using the parameters detailed in Section 3.2.2. The effectiveness of this direct-imaging approach with the UXI detector is demonstrated in the bottom row of Fig. 3.3, in which laser-driven shock compression was captured by a scintillator-based UXI detector. A

comparison between the top and bottom row of Fig. 3.3 illustrates how the direct-imaging geometry is suited for the task of uncovering details in the shock front over multiple frames while providing a sufficient image contrast-to-noise ratio.

As seen in Fig. 3.3g, after the interaction with the compression wave, the void's edge appears at a different position, further within the sample compared to its initial rest position. The void's edge appears to be in front of the shock front itself, which suggests that the shock wave accelerates as it traverses the void, dragging its edges at a higher speed with respect to the surrounding SU-8 material; this "jetting" is expected, as the impedance mismatch between the SU-8 and the air should result in an increase of Us. Thus, the data demonstrates that the interaction with inhomogeneities within the sample, in this case a micron-sized void, can affect the shock wave propagation, eventually resulting in jetting and possibly giving rise to other instabilities.

The use of the direct-imaging geometry clearly enhances our ability to capture features behind the shock-wave and to provide sufficient phase contrast to visualize without overshadowing the interaction of the shock front with the embedded voids. Although XPCI imaging in the holographic regime is a useful experimental technique for a variety of applications, direct-imaging provides an alternative way to visualize features within or behind the shock front, from the dense compressed region. Moreover, this configuration still enables imaging of ultrafast dynamics at the nanosecond time scale [81].

3.4 Analysis: Flat-field correction, xRAGE simulation comparison, and mass density extraction

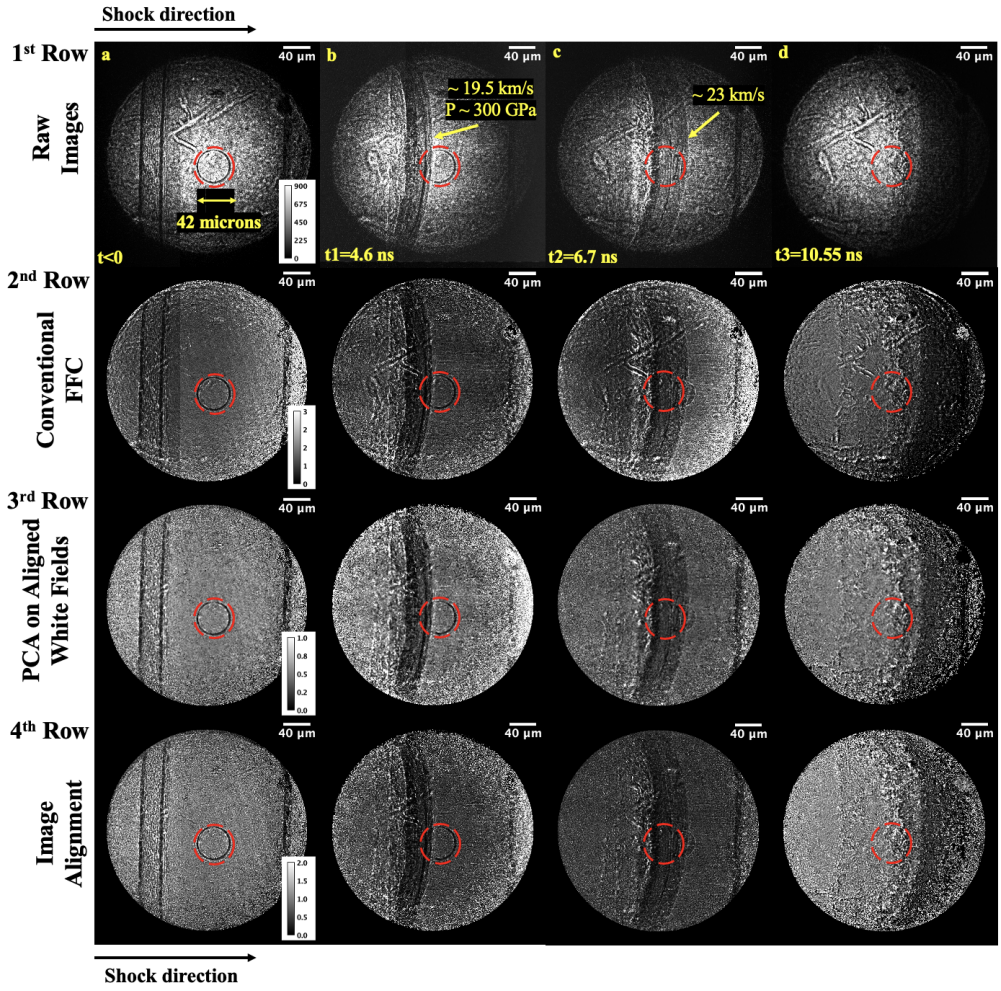

Figure 3.5 A 10 ns flat-top pulse was used to shock the sample and images were collected on the UXI detector. Each row contains a sequence of four normalized FFC images of a single sample. For each row, the images are scaled based on the given scale bar in the left panel. The scale bars are given as I/I0, where I is the original image and I0 is the image used to divide and give the normalized flat-field image. The dashed red circles indicate the location of the 42 μm diameter hollow silica void as the shock propagates through the SU-8 material. **First Row (a-d)**: Raw images obtained for this experimental campaign. **Second Row**: Conventional flat-field corrected (FFC) images produced by dividing the dynamic images with the average white field. **Third Row**: FFC images generated by applying principal component analysis (PCA) on only the registered white fields generated by the image alignment method. **Fourth Row**: FFC images using only the image alignment method.

3.4.1 Flat-field correction (FFC) techniques

For x-ray imaging experiments, FFC is a necessary requirement for image analysis since image quality is degraded by fixed-pattern noise on the detector and random noise from the XFEL pulses, a characteristic that naturally occurs from the XFEL self-amplified spontaneous emission (SASE) mode [82]. FFC is a technique utilized to mitigate image artifacts arising from variations in detector sensitivity and distortions in the optical path not caused by the sample [83]. Conventionally, FFC is computed by first obtaining two sets of images, namely, a series of images with only the beam illuminating the detector (white fields, no sample) and a series of images without any beam illumination (dark fields). Once these images are obtained, a sample is normalized with the average white field image after the average dark field image is computed and subtracted from each white field image. Ideally, this standard calibration procedure reduces fixed-pattern noise and intensity variations in the x-ray beam before the sample, resulting in sample-induced only intensity variations. However, due to the large intensity fluctuations on a shot-to-shot basis due to the stochastic nature of the XFEL, more advanced FFC methods must be used to estimate each pulse's flat field contribution. The ineffectiveness of conventional FFC compared to other methods is displayed in the second row of Fig. 3.5. We test the performance of principal component analysis [68] combined with image alignment to generate flat-field corrected images where conventional flat-field techniques based on average illumination fail.

Principal component analysis (PCA)

To overcome the problem of fluctuating intensity between frames for FFC, we implemented PCA demonstrated by Hagemann et al. [68], which is a dimensionality reduction or feature extraction technique that reduces the dimensionality of large data sets so they can be more easily interpreted and information loss is minimized [68, 84–86]. Dimensionality is reduced by projecting the data to lower dimensions, which are interpreted as principal components (PCs). These PCs can be thought of as effective modes of SASE beam fluctuations and instability. A linear combination of all the principal components completely describes the original data set. However, a few components contains a majority of the information from the original data set, so not all components are required for FFC. More components gives higher accuracy, but at the cost of additional computation time.

To account for long term drifts of the XFEL, and to apply proper FFC for sets of dynamic images, we collected white field images prior to every dynamic shot [68]. For selected dynamic runs, we used PCA to search for the maximum variance between the collected white fields, which would indicate major contributing factors to noise and x-ray pulse deviations. PCs are constructed and ordered based on what caused the most variation between each of the white field images, i.e., each component is orthonormal and can be considered an eigenvector pointing in the direction that describes the most variance in the data set. Every eigenvector has an associated eigenvalue, a scalar that reflects the amount of variation that the eigenvector accounts for (higher eigenvalue means higher the variation). Visualization of these components are shown in the supporting information. For example, component one corrects for the intensity variations between pulses, which is known to strongly fluctuate on a shot-to-shot basis for XFELs. The subsequent components account for and

correct the pointing stability (center of mass of the beam being shifted between each image), which is another contributing factor that describes the SASE pulses. Therefore, projecting the white fields to lower dimensions with PCA gives a unique representation of what contributes most to XFEL beam behavior, so FFC images can be generated.

The number of PCs chosen for best FFC results are based on two considerations: 1) the number of components cannot exceed the number of white fields obtained, and 2) we kept only the first five principal components since this amount resulted in a majority of the variance and reduced computational time. For our void-shock image sequence, we collected a total of 40 white fields prior to the dynamic shot, but only 27 were used since some white fields were corrupted or had low intensity. For the void-shock image displayed in the bottom row of Fig 3.3, we used five principal components accounting for $\sim$96% of the total variation. Images incorporating this technique are shown in the supporting information. Once PCs were obtained, we constructed weights by projecting the dynamic image that needed FFC on the basis given by the components. When the weights were obtained, a synthetic flat-field image was created which is used to normalize our dynamic image. Prior to computing PCA, spurious pixels were replaced by the median value of the image to improve FFC results. Additionally, we set negative pixel values to 0 as they were not physical. To further aid in FFC, we performed image alignment to correct for high frequency variations.

Image alignment

PCA is effective in correcting pulse-to-pulse variations in the x-ray beam intensity. However, the combination of pulse-to-pulse variations in the x-ray beam energy, long-pulse laser shockwave, shift artifacts in the images created from defects in the lenses, which PCA cannot correct. To alleviate this problem, we track the displacement of the high frequency intensity modulations before and after the object is inserted into the optical path. To determine these relative shifts, the diffeomorphic demon's algorithm [69, 70] was used to perform a nonrigid image registration between the white fields and dynamic images. This algorithm solves an unconstrained regularized minimization problem by reducing the difference in intensity between the white fields and dynamic images while penalizing for roughness in the displacement field.

For successful FFC we first registered all of our white fields to the first white field event. After that, we formed a single averaged white field image from these aligned fields. The averaged white field were aligned to each dynamic image to compute the displacement field. This was then applied to the original white fields for each dynamic frame. We divided our dynamic shots with the aligned white fields, generating FFC images shown in the bottom row of Fig. 3.5.

Combining PCA and image alignment

We combined image alignment and PCA to account and correct for both high- and low-frequency variations. The order in which we applied these techniques was based on a systematic comparison of the image alignment method and PCA on obtained white fields. For the best FFC results, we determined that PCA should be applied after image alignment. For each dynamic frame, the white

field images were registered and aligned as described in Section 3.4.1. Furthermore, as described in Section 3.4.1, we performed pixel correction and then used these corrected and registered white fields as our "new" white fields for the PCA algorithm to synthesize FFC images. Here, only five principal components were used, accounting for $\sim$96% of the total variation in this "new" white field data set. These images are shown in the third row in Fig. 3.5. Overall, the combination of these techniques yield clearer, visible features within the images compared to each method on its own. It should be noted that there are still artifacts present in all the images in Fig. 3.5 regardless of method because of strong phase-contrast effects distorting the artifacts beyond which can be corrected by using these methods.

3.4.2 Experimental comparison to XPCI simulations

A void-shock interaction, or generally known as a shock-bubble interaction (SBI), is a standard configuration when analyzing shock-accelerated inhomogeneous flows [11]. Even in this idealized sample configuration, several complex mechanisms occur when a shockwave impacts a void, giving rise to three main processes that occur within the multimaterial medium: compression/acceleration, shock reflection/refraction, and baroclinic vorticity generation [11]. These processes are nonlinearly coupled to each other, forming complicated features based on disordered rotational motion and turbulent mixing that arises during compression. The recent advancement of cameras, such as the ultrafast Icarus V2 camera that we have implemented, enables direct observation of inhomogeneous flow evolution at the nanosecond time scale caused by impulsively driving cavities within ablator materials. Here, we compare our experimental four frame compression of a single sample to its

corresponding simulated multi-frame XPCI void-shock images to provide insight into material behavior at the nanosecond and micron scales.

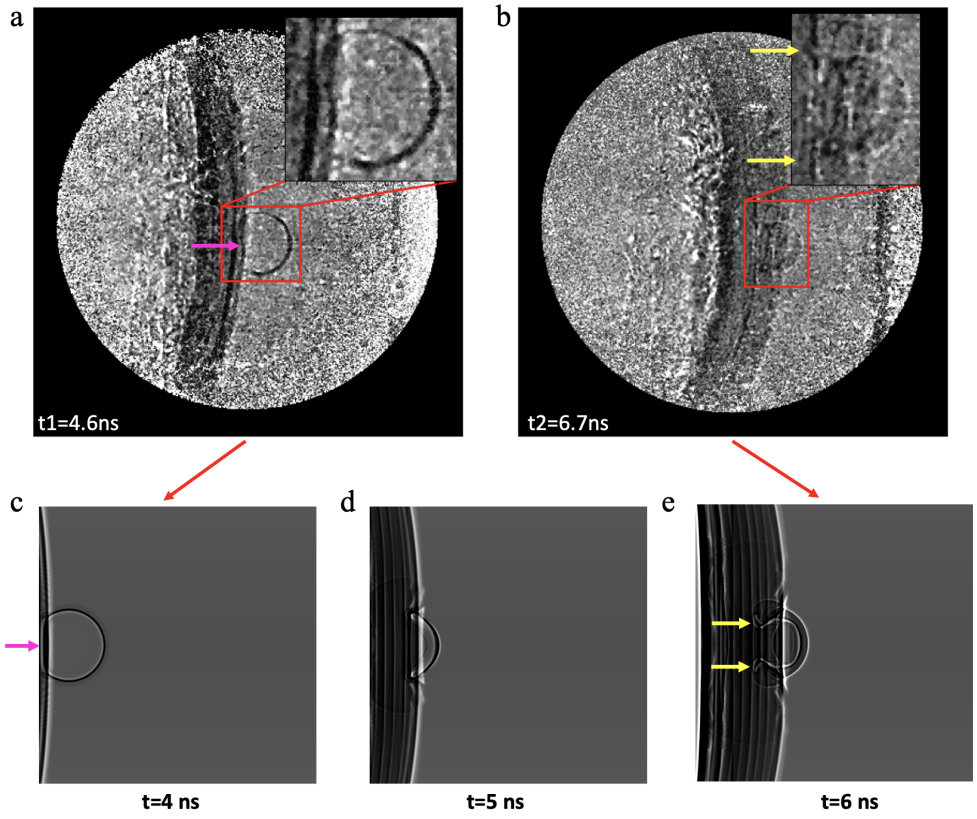

Figure 3.6 **Top Row**: Experimental intensity images capturing void-shock interaction. Panel (a) and panel (b) displays shock propagation 4.6 ns and 6.7 ns (2.1 ns after panel (a)) after the shock wave impacts the medium. The insets in panel a and b show a zoomed in version of the void-shock interaction for better visibility. The purple arrow in panel (a) indicates the mass being stripped off the SiO_2 shell while the yellow arrows in panel (b) indicate the curl up at the edges of the void as a result of the shock wave propagating through it. **Bottom Row**: The red arrows indicate the simulated intensity images that correspond to the experimental intensity images depicted in the top row. Panel (c) shows 4 ns after a shock wave interacts with the medium while panel (e) displays the intensity after 6 ns, corresponding to nearly the same time step experimentally. Panel (d) is an intermediate time step (5 ns) that occurs 1 ns after the first frame. **Note**: We recognize that the void-shock interaction is aligned in simulation, while it is not the case for the experimental images. The experimental misalignment was unintentional and arose due to experimental conditions at the time. However, we attempted to match simulation and experiment as best as possible.

A two-dimensional simulation was performed in xRAGE, a Los Alamos National Laboratory (LANL) Eulerian radiation-hydrodynamics code, to study the effects of shock propagation and instabilities that occur in a single material containing a micro-void. xRAGE is an Eulerian finite volume code that solves the compressible Euler equations with adaptive mesh refinement in 1-, 2-, and 3-dimensions, and SESAME tabular equations of state [87]. Radiation transport and strength effects were neglected in our simulations. We chose specific parameters for this simulation to best match our experimental conditions. The parameters are listed in Table 2 in the supporting information.

This simulation provided a model to help us understand void collapse evolution within the SU-8 medium. A movie of 160 density images with temporal resolution of 0.1 ns was provided, revealing collapse dynamics occurring on timescales shorter than the frame rate of the UXI camera. Density images corresponding to experimental images at similar time frames were inserted into the supplemental information for reference. To provide a one-to-one correspondence between experimental data and simulation, we calculated the phase and attenuation maps by performing a forward Abel transform on the simulated density images. Once these maps were generated, we used the angular spectrum method to numerically propagate them a distance L, an effective propagation distance determined in Section 3.4.3 and the supplemental information. Among these images, a few were selected based on how well they resembled our experimental data at a specified time interval. Fig. 3.6 shows how closely the XPCI simulation resembles the void-shock evolution of the experiment. The simulated image in panel (d) was included to explain what we would expect to see experimentally if higher temporal resolution was obtained. Each simulated frame (panels (c)-(e)

in Fig. 3.6) shows progressive movement of the shock front through the void, clearly displaying the void-shock evolution at different time steps. The first simulated frame (panel (c)) at 4 ns is comparable to the experimental image at 4.6 ns (panel (a)), when our shock initially strikes our void. As the shock enters the void, it accelerates, traveling faster than the unperturbed exterior shock. One nanosecond later (panel (d) in Fig. 3.6), the interior shock reaches the far side of the void, and begins to exit the far side of the bead. At 6 ns in the last simulated frame (panel (e)), corresponding to 6.7 ns experimentally (panel (b)), the remaining bead material has been swept up by the portion of the shock that traversed the void, and some material is now displaced ahead of the oncoming unperturbed shock. The distribution of this bead material is in good agreement with the second frame from the UXI camera (panel (b)). We note that there is an aliasing effect that starts to develop on the left side of Fig. 3.6e and this has insignificant influence when qualitatively comparing simulated and experimental images.

Using the known EOS for polyimide as described in Section 2, we estimate the pressure attained in each experimental image; propagation of a shockwave leads to void compression and results in a jump of pressure, temperature, density, and translational velocity. Translational void velocity is noticeable by comparing the red dashed circles in Figs. 3.4 and 3.5. During each time step in Fig. 3.5, it is seen that the void is displaced from its original location. By examining the purple arrow in Fig. 3.6a, we see mass is stripped off the original bubble and mixes with the surrounding heated up fluids. This process continues as the shock wave propagates through the void and ablator material. A purple arrow is also included in corresponding simulated image for comparison (see Fig. 3.6c). Vorticity is seen on the edges of the void in Fig. 3.6b, where yellow arrows are used

to label the resulting curl up. Yellow arrows are included in the simulated image (see Fig. 3.6e) for comparison to the corresponding experimental image. We generated an average shock speed of Us$\sim$19.5 km/s, which corresponds to a pressure of 300 GPa as estimated from the polyimide equation of state [75, 88].

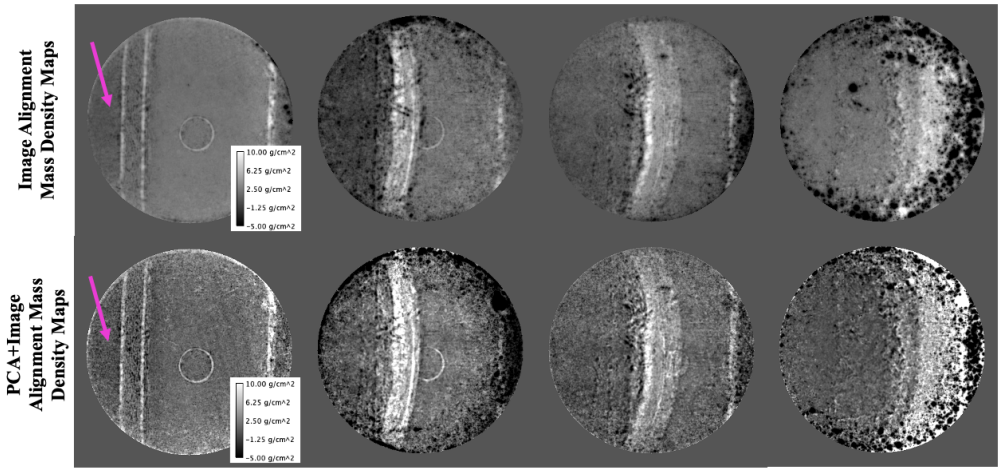

Figure 3.7 We use the transport-of-intensity (TIE) based approach to analytically solve for the average projected mass density (areal density) of the multi-material medium containing SU-8 and the hollow SiO_2 void before and during shock compression. These images are still very preliminary. The scale range in the left panels are used for all the images. The purple arrows in the left column indicate portions of the sample which contain air only. Each image was rescaled such that the average mass density (areal density) containing air only is 0. **Top Row**: TIE based approach applied to the image alignment technique. **Bottom Row**: TIE based approach applied to the combination of the PCA and image alignment technique.

3.4.3 Application of the transport-of-intensity (TIE) based method

The direct-imaging geometry enables images to be recorded in the near-field regime. In this regime, the image provides a "direct" resemblance of the object. In our study, this allows us to visualize both the void and shock front without being masked by large Fresnel fringes and corresponding

refractive dark band effects. Furthermore, direct-imaging linearly relates the image intensity and properties of the object. We exploited this relationship by using a TIE based approach to calculate mass density maps of the shock-induced void collapse displayed in Fig. 3.7.

In comparison to traditional propagation-based near-field imaging geometries, where there are no optics between the sample and detector, direct-imaging has additional layers of complexity when analyzing the images. First, images recorded in the direct-imaging geometry are modified by both propagation-based phase effects and absorption of X-rays in the compound refractive lens. Several works have investigated these effects both theoretically and experimentally [89–92]. In our experimental setup, we employed Be-CRL. This resulted in a differential absorption between the center and edge ($\sim$40 μm from the center) of the lens of $\sim$3.5%. However, this differential is negligible compared to sample-induced intensity variations. We can therefore use equations describing free-space wave propagation to relate the image intensity to the object wavefield [93]. In this study, we chose the continuity TIE equation and re-derived the single image phase retrieval algorithm developed by Paganin et al. [94] to solve for the average mass density ($\int \rho\, dz$) of the sample along the direction of the x-ray beam from a single flat-field corrected image I of pixel size W:

$$\frac{\int \rho\, dz}{T} = -\frac{1}{\mu T} \log \left[F^{-1} \left\{ \frac{F\{I\}}{\frac{2L\delta}{\mu W^2} \left[\cos\left(W k_x\right) + \cos\left(W k_y\right) - 2 \right]} \right\} \right] \tag{3.2}$$

In deriving Eq. 3.2, we assumed spatially coherent, monochromatic x-rays and their interaction with the sample when it obeys the projection approximation. In addition, the sample is composed of a single material with a complex refractive index 1-$\delta\rho$+$i\mu\rho$, where μ is the mass attenuation

coefficient per mass density, δ is the refractive index decrement per mass density. $k_\perp = (k_x, k_y)$ is the transverse spatial frequencies in frequency space corresponding to the image real space coordinates (x,y). These coordinates are related by the Fourier and inverse Fourier transforms, F and F^{-1}, respectively. L presents the distance of the detector from the Be-CRL image plane, which means L can be positive or negative. T is the thickness of the sample along the x-ray propagation direction and is assumed to be constant. We note that although the mass attenuation coefficient changes with temperature, its effect is insignificant unless extreme temperatures are involved. Specifically, for our experiment, changes to the material attenuation coefficients in our warm dense matter regime are no more than 0.1% - 1% for silicon and carbon based on FLYCHK calculations [95] for temperatures of 1–5 eV. Therefore, changes in the material attenuation coefficients are negligible and Eq. 3.2 remains valid for our experiment.

Directly measuring L is non-trivial because of difficulties in accurately measuring the Be-CRL effective focal and image planes. To overcome this challenge, we performed XPCI simulations using the angular spectrum method of a SiO_2 shell embedded in SU-8 for different L and SiO_2 shell thicknesses. These results are contained in the supporting information. We compared Fig. 3.5 to these simulated images, and we concluded from the presence of a distinct dark band with bright bands on either side seen in Fig. 3.5 that $L \geq 0$ mm. This results in much smaller numerical errors as opposed to when L is negative, where there will be a division by zero in Eq. 3.2. Consequently, L can be tuned within the domain $[0, \text{inf})$ until the Fresnel fringes in the image are removed and applied to the other images. Also, due to the pulse-to-pulse fluctuation in the x-ray that was not fully corrected with our flat-field correction method, we rescaled each image in Fig. 3.7 such that

the average mass density containing air only (indicated by the arrow in Fig. 3.7) is zero.

Eq. 3.2 can accurately solve for single material samples, but our sample is composed of two materials, SiO_2 and SU-8. While there are single image multi-material TIE-based phase retrieval algorithms [96], these algorithms assume only one of the materials has spatially varying properties. Therefore, we chose to tune Eq. 3.2 to calculate the average mass density of SU-8. This allowed us to compare the average mass density of the shock front with the xRAGE simulations. In regions containing the void, it is slightly over-blurred and not quantitatively correct; however, image noise surrounding it was inadvertently suppressed and improves visual comparison with the xRAGE simulations.

Fig. 3.7 shows the average mass density maps of the two methods shown in the bottom rows in Fig. 3.5. The speckle-only average mass density maps display less high frequency artifacts than that of PCA combined with speckle. However, without PCA there is still low frequency variations present due to imperfect normalization against the stochastically varying x-ray beam intensity profile. We suspect this is because of the small number of white fields that were available for PCA. In future experiments, we plan to record more white fields for PCA before combining with speckle to remove both low- and high-frequency artifacts in the average mass density maps. There are regions in which the average mass density is negative, particularly towards the edge of the x-ray beam where the photon count is low or where portions of the image are noisy after FFC. Towards the center of the x-ray beam, the average mass density of the shock wave is quantitatively comparable with xRAGE. The TIE assessment presented here is just a preliminary test of this method. In future works, we plan to generalize Eq. 3.2 to solve for multiple material properties by incorporating

advanced model-based iterative reconstruction methods that also account for Poisson noise by, for example, imposing positivity constraints to ρ.

3.5 Conclusion

The UXI platform demonstrated here has the potential to revolutionize HEDP with the capability to capture multiframe material dynamics of a single sample at the nanosecond time scale. We have successfully captured a series of three dynamic frames of void-shock evolution with 700 nm half-pitch resolution over 8 ns in a direct-imaging geometry. Our results advance our understanding of void collapse in extreme states and demonstrates the wide applicability of the UXI camera. These results provide fundamental insight on how material inhomogeneities, such as micro-voids, influence material properties during the propagation of a laser shockwave. Moreover, to quantitatively understand void-shock interaction and how the material structure evolves over several nanoseconds, we utilized a TIE-based phase retrieval method to give us the average projected mass density of the sample. The UXI has demonstrated that pressure regimes of several Mbar can be imaged, paving the way for understanding physics over shorter time-scales for non-repeatable ultrafast phenomena. Our technique for void characterization during laser shock compression will contribute to minimizing instabilities that occur at the micron scale in ICF experiments.

Next generation gallium arsenide (GaAs) sensors will extend this technique to higher x-ray energies, expanding burst-mode science experiments. Although this detector was designed for HEDP experiments that require nanosecond sampling, it can acquire data at nanosecond or sub-nanosecond

time scales, improving data acquisition speed and overall operational efficiency. Moreover, with improvements to the camera, particularly the quantum efficiency, will lead to improved accuracy in quantification of the projected average mass density, enabling us to understand nanosecond time evolution of matter in extreme conditions.

Chapter 4

Phase retrieval and future work

This thesis has provided two manuscripts which have successfully demonstrated for the first time the implementation of an UXI detector to capture nanosecond frame rate, multi-frame, laser shockwave dynamics of a void-bearing sample in a holographic and direct x-ray imaging configuration. In the first manuscript presented in Chapter 2, $\sim$8 keV energy XFEL pulses provided by LCLS illuminated our samples and introduced extreme phase-contrast effects that caused Fresnel fringes to obscure details behind and along the shock front. Forward simulations indicated that higher energy XFEL pulses were required to reduce these phase-contrast effects. Although higher energies could have provided insight into the dark band structure caused by phase-contrast effects, the study in Chapter 3 shows that switching to the direct imaging configuration minimized the influence of the Fresnel fringes by effectively reducing the propagation distance between the sample and the detector, thereby, making features directly recognizable. The UXI platform demonstrated here has shown that the holographic and direct-imaging techniques with the UXI can be applied to study void-shockwave

interactions on nanosecond timescales, which is crucial to advancing ICF science. Moreover, these methods can be used to expand our understanding of the underlying physics involved with other non-repeatable ultrafast phenomena. This section reviews coherent x-ray imaging (CXI) techniques that can be used to extract quantitative information (i.e. phase information and areal density) from images captured at LCLS and potential future projects that will implement these methods to solve ICF-related challenges.

4.1 Coherent x-ray imaging (CXI) and phase retrieval techniques

Coherent x-ray imaging (CXI) is a lensless 2D or 3D imaging technique that combines oversampling and phase retrieval methods to reconstruct an object exit surface wave (ESW) from its x-ray diffraction image [97–99]. An advantage to this technique is that the spatial resolution of the recovered image is limited only by the spatial frequency of the diffracted waves (i.e. the higher the frequency, the smaller the features we can visualize) and the image is aberration-free [100, 101]. Another important aspect of CXI is its ability to probe dynamic phenomena with high spatio-temporal resolution [100], which is of significant interest given the images obtained in this thesis and other images captured using the LCLS XFEL setup at the MEC instrument.

The general process for CXI involves quasi-monochromatic coherent x-rays illuminating an object and collecting its diffracted waves on a detector. However, the oscillating period of x-ray radiation is at such high frequencies ($\geq 10^{16}$ Hz) that detectors can only respond to the intensity,

which results in a loss of phase information about the illuminated object. In other words, details are lost about the individual scattering events that took place inside the sample. This is commonly known as the "phase problem" [102]. Recovery of the Fourier phase is crucial since it contains more information about the object than the Fourier magnitude [99], which can be seen in the synthetic example shown in Fig. 4.1. This lost phase information results in an ill-posed inverse problem when attempting to reconstruct the ESW of the object from its intensity pattern alone. Therefore, various phase retrieval methods are implemented to solve this problem [71, 97, 99, 102–117].

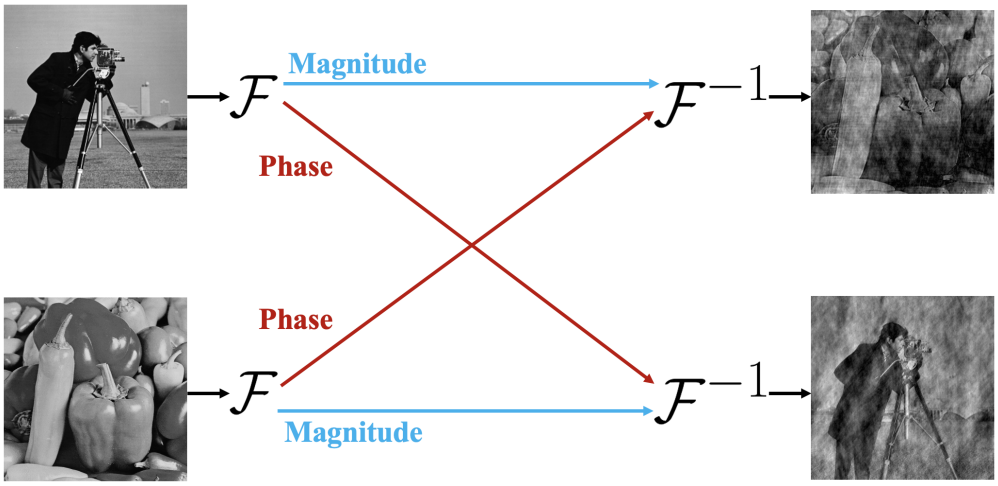

Figure 4.1 Two images presented on the left are Fourier transformed. The phases are swapped and then an inverse Fourier transform is performed. This result indicates that the Fourier phase contains more information than the Fourier magnitude, which emphasizes the importance of recovering phase information. Therefore, phase retrieval techniques are required for image recovery. This image was modified from Shechtman et al. [99]

Typically, there are two classes of algorithms that can be used to solve the inverse problem: iterative projection algorithms (alternating projections) and gradient descent algorithms [104, 118]. Methods based on alternating projections (AP) were pioneered by Gerchberg and Saxton [119] and Fienup [102, 103, 120–122]. In AP methods, a complex image is reconstructed by imposing

constraints on the Fourier (diffraction) and real (imaging) planes. The advantages in using these types of algorithms arises from its simplicity in implementation and a few finely tuned parameters that are required. However, AP methods suffer from low imaging quality if few diffraction patterns are recorded and if noise is present in the recorded images [123]. To overcome these challenges, recent improvements and additions to existing algorithms have been implemented [99, 117, 124]. Even with more advanced AP algorithms, difficulty remains in retrieving phase information from few to single diffraction images. Methods based on gradient descent aim to minimize an objective function (fidelity term) that ensures that the object estimate is consistent with the given diffraction pattern obtained. In general, this method is more flexible and powerful than alternating projections [118, 123]. The reason for this is twofold: 1) one or more regularization terms can be added to the fidelity term, which enforces particular solutions based on prior knowledge of the sample; and 2) the data fidelity term can be constructed based on the type of noise introduced, making these algorithms robust to noise. A list of a few common AP and gradient descent techniques with their respective advantages and disadvantages are listed in Table 4.1. This table is not comprehensive but aims to introduce common algorithms that are commonly used in literature.

Table 4.1 List of Phase Retrieval Methods

Method	Advantages	Disadvantages/ Limitations	References
Error Reduction (ER)	– Theoretically leads to convergence	– Requires tight support region – Very slow convergence – Takes many iterations – Results tend to be trapped in local minima if any noise is present – Solutions tend to stagnate for complex-valued signals	[102], [121], [122], [99]
Hybrid Input-Output (HIO)	– Contains feedback information concerning previous iterations, reducing the probability of stagnation – Improvement of convergence when used in conjunction with the ER algorithm	– Requires tight support region – No proof of convergence – Results tend to be trapped in local minima if noise is present – Solutions tend to stagnate for complex-valued signals	[102], [106], [125], [126], [99]

Oversampling Smoothness (OSS)	– Outperforms ER, HIO, and the combination of ER+HIO. – Robust to noise	– Requires a tight support region. – Details in the reconstruction are blurred – Tunable spatial frequency filter causes solution to oscillate hundreds of iterations after initial convergence	[117], [99], [127]
Guided Hybrid Input-Output (GHIO)	– Higher probability in escaping local minima compared to HIO – Fast convergence rate – Works well for complex-valued objects	– Requires a tight support region. – Computationally demanding – Probability to reach the global minimum depends heavily on the random initial phase values	[108], [99], [128]
Difference Map (DM)	– Very fast – Robust – Can effectively avoid stagnation	– Requires tight support region – No useful bounds on the number of iterations required to find a solution (takes unknown amount of iterations for convergence)	[110], [125], [129]
Relaxed Averaged Alternating Reflections (RAAR)	– Easy to implement – Analytically tractable – Rapid convergence – Avoidance of local minima	– Requires tight support region – No proof of convergence – Solutions tend to stagnate for complex-valued signals	[113], [99], [110], [130]

Ptychography	– No support region required – Robust against noise – Applicable to extended objects – Simultaneously reconstructs probe and object – Fast convergence rate – Tolerant to incoherence	– Scanning process is extremely slow – Works only with static samples – A single-shot version of ptychography has only been implemented with visible and near-visible wavelengths	[111], [112], [131]
Transport-of-Intensity (TIE) based method	– Can apply to materials that are spatially varying – Requires only one intensity image – It is a computationally-simple unique closed form deterministic solution to the twin image problem – Simple implementation – Computationally fast – Robust to noise	– Applies only to single element materials – Sample-to-detector distance must be small (i.e. Fresnel number must be large compared to unity)	[71], [94]

Gradient Descent Based Algorithms	– Computationally efficient for most algorithms – Regularization terms improve imaging quality (i.e. suppresses artifacts and preserves fine details) – Regularization terms reduce number of measurements required	– More finely tuned parameters are required – Some machine learning implementations require extensive computational resources and long processing times	[132], [104], [133], [134], [135], [136], [137]

4.2 Future research with single-shot imaging phase retrieval

Generally, retrieving phase information without *a priori* knowledge of the sample requires multiple intensity measurements [96], which can be obtained by varying axial distances, illumination angles, illumination wavelengths, modulation patterns, or probe positions, ensuring numerical recovery [104, 111, 138, 139]. However, if *a priori* information is known, it is possible that phase information can be recovered from a single diffraction image [138], and a combination of iterative methods listed in Table 4.1 can be utilized to solve the inverse problem. Even with these algorithms, the problem of recovering a phase map of the illuminated sample remains non-trivial for a couple of reasons: 1) a single image captured in-line requires a proper forward model that best represents our experimental data to initiate a good starting phase estimate of the object (so we do not get caught in a local minimum); 2) the stochastic nature of the XFEL introduces noise into the images,

which degrades the quality of the reconstruction significantly; and 3) multiple materials are spatially varying due to the shockwave propagating through the sample, which adds additional complexity to the reconstruction process since current multi-material phase retrieval algorithms support only a single spatially varying material [71, 93, 96]. Future work will use a combination of phase retrieval techniques to recover the phase information accurately from single-shot images acquired at LCLS, which can be used to obtain void-shock areal density distributions and ultimately progress ICF science. Even though the TIE-based method in Chapter 3 gave reasonable areal density results, this particular technique suffers in three aspects: 1) This method in unstable and yields negative density in certain areas of the image, which is not physical; 2) It is extremely sensitive to noise, which can degrade and dramatically alter the output; and 3) This technique was designed only for a single spatially varying material while our sample is composed of two spatially varying materials, SiO_2 and $SU8$, indicating that we can only accurately obtain phase information for one of the two samples. The combination of these problems diminishes the quality of the output, which indicates a need for additional methods and refinement.

Even though only a single intensity image is required when sufficient *a priori* information is known, additional considerations still arise when recovering the ESW of the sample, namely, low signal-to-noise [28, 33, 82], the twin image problem [106, 121, 140, 141], and oversampling [106, 107]. These factors cause an increase in complexity which will require using a combination of phase retrieval algorithms, phase unwrapping tools, and image alignment techniques to generate successful reconstructions. Once a working phase retrieval algorithm is constructed, we can implement it to the vast amount of existing data that has been obtained from previous experiments conducted at the

LCLS MEC instrument.

4.3 Summary and Outlook

This section has summarized the potential of the UXI camera and how it can impact ICF experiments. A brief overview of CXI was given along with a compact list of common phase retrieval algorithms required to obtain phase information from single-shot intensity images. To resolve the ill-posed inverse problem, several essential actions have been proposed and are currently being implemented. Retrieving phase information from a complex dynamic image will advance the study of ultrafast phenomena and continue to progress ICF science.

Appendix A

Supplemental information: "Multi-frame, ultrafast, x-ray microscope for imaging shockwave dynamics"

Abstract. This supplemental paper contains additional visualizations concerning experimental parameters between different experiments, flat-field correction (FFC), principal component analysis (PCA), a table describing the parameters used in our 2D xRAGE simulations, and images displaying differing SiO_2 shell thicknesses and propagation distances for the TIE based phase retrieval method.

A.1 Results: Comparison of XPCI imaging in the holographic and direct-imaging regime under shock compression

Table A.1 Experimental Campaigns for Void Collapse

Experiment	XFEL Energy	Be CRLs Info	Camera
LV08 (experiment 1)	8.23 keV	– Placed before the sample – 40 Be CRLs – 29X magnification	– UXI – Placed 4.583 m after the sample
X437 (experiment 2)	8.28 keV	– Placed after the sample – 25 Be CRLs – 20X magnification	– Andor Zyla – Placed 4.5 m after the sample

X493 (experiment 3)	9 keV	– Placed after the sample – 52 Be CRLs – 40X magnification	– UXI – Placed 4.3 m after the sample

Table A.1 describes the three experimental campaigns described in the main text. Column 1 describes the experimental campaign while columns 2-4 include the associated parameters and detector used for a particular experiment. Details about the current experimental campaign described in the main text can be found in the last row of Table A.1.

A.2 Comparison between flat-field correction (FFC) methods

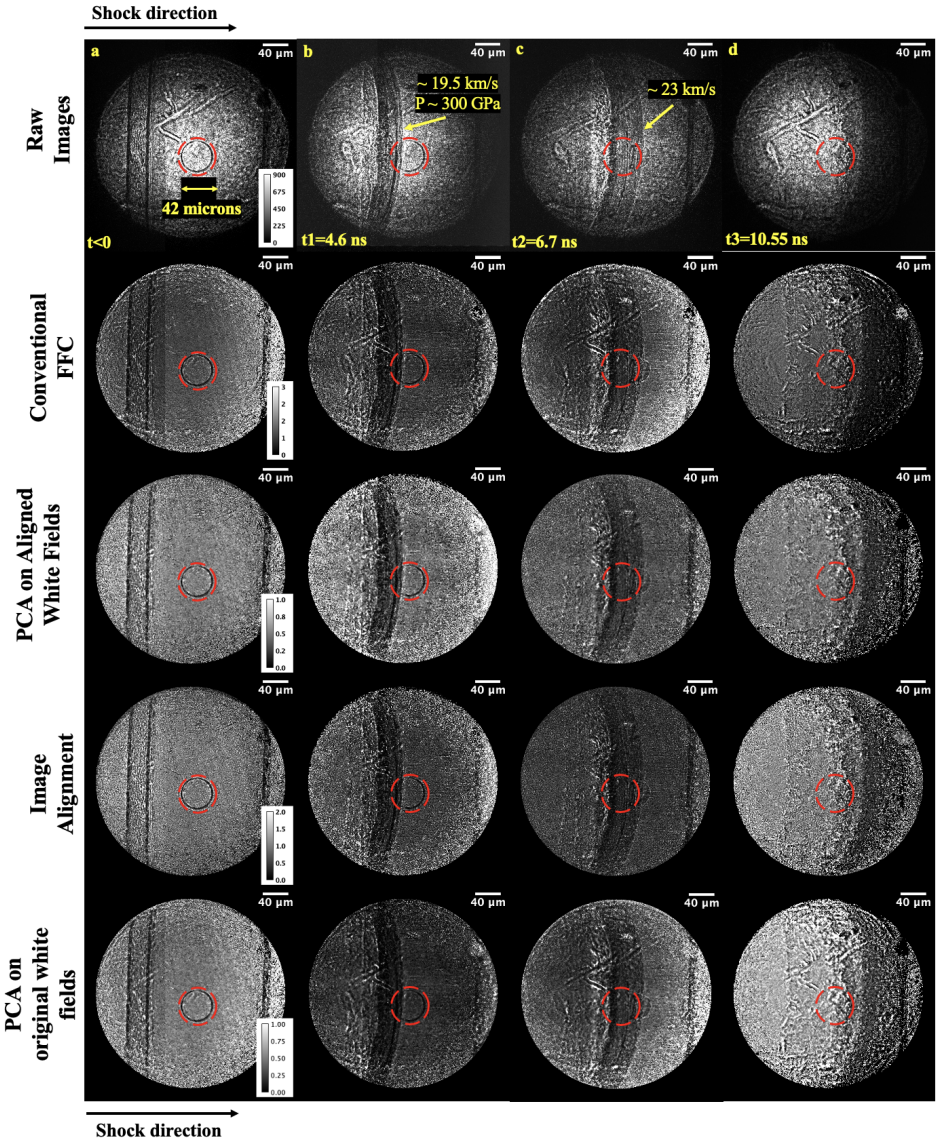

Figure A.1 Each row contains a sequence of four images of a single sample. For each row, the images are scaled based on the given scale bar in the left panel. **First Row (a-d)**: Raw images obtained for this experimental campaign. A 10 ns flat-top pulse was used to shock the sample. The dashed red circles indicate the location of the 42 μm diameter hollow silica void as the shock propagates through the SU-8 material. **Second Row**: Conventional flat-field corrected (FFC) images produced by dividing the dynamic images with the average white field. **Third Row**: Principal component analysis (PCA) was applied using only the registered white fields generated by the image alignment method. **Fourth Row**: FFC images applying only the image alignment method. **Fifth Row**: FFC images applying PCA on the original white field images. **Note**: For the third and last row, five principal components were used.

Fig. A.1 displays the same figure as in the main text, but now it includes principal component analysis (PCA) in the bottom row. Again, five principal components were used, which explains ∼96% of the total variation of the data. Comparing these images to the third row demonstrates the necessity of the image alignment technique to correct for the high frequency variations caused by the lens and shockwave.

A.3 Principal component analysis (PCA)

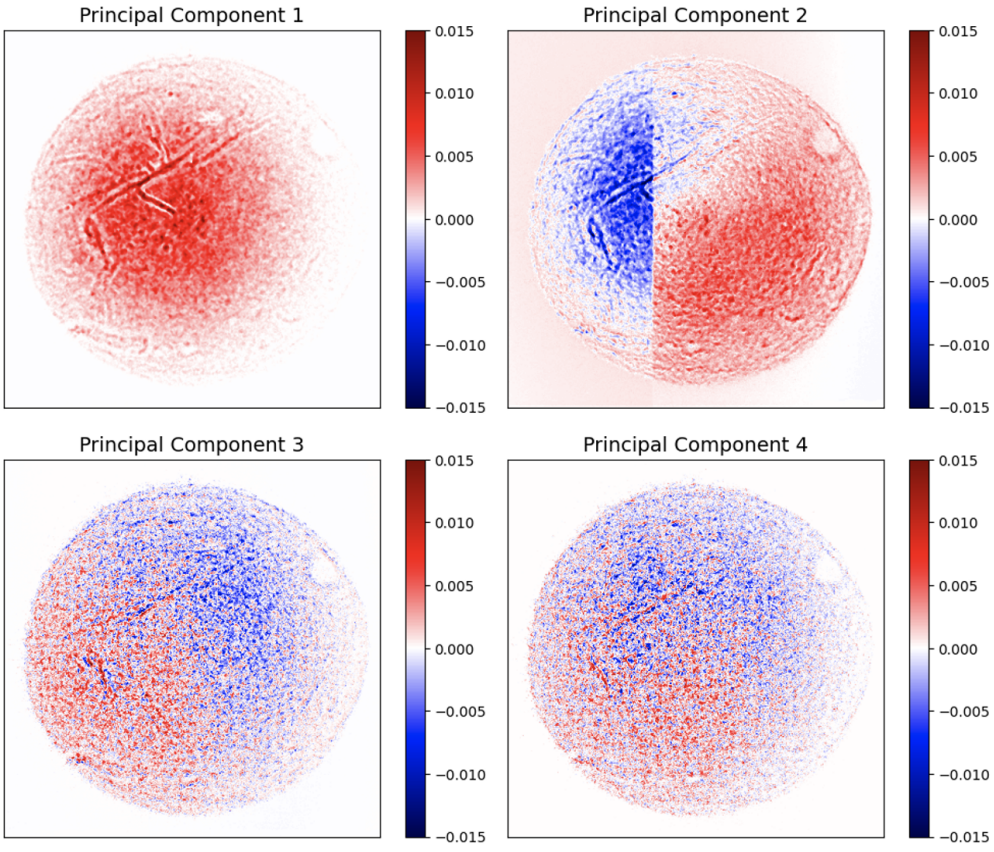

Figure A.2 Four principal components obtained from applying PCA on the aligned white fields generated by the image alignment technique. These principal components illustrate the major contributions of our XFEL pulses in descending order.

Principal component analysis is an advanced method for FFC and its capabilities have been demonstrated in Fig. A.1. Fig. A.2 displays four principal components obtained by applying PCA on white fields generated by the image alignment technique. Both methods were incorporated since PCA can fix low frequency variations such as pulse-to-pulse variations and image alignment corrects for high frequency variations such as lens induced defects on the sample projected onto the camera. This reduced the amount of low- and high-frequency fluctuations in the images so quantitative information can be extracted with minimal error. The varying intensity between pulses, which is a common feature of XFELs, is captured in principal component 1 in the top left panel in Fig. A.2. It was calculated that this component contains 91% of the total variation. This confirms that the intensity between pulses contributes to the most variation compared to other factors. The subsequent components captures pointing (center of mass) of the beam, dirt, and shifting features. Principal component 2, which describes the pointing of the beam and camera gain, is the next highest contributing factor and contains 4.24% of the total variation. Principal components 3 and 4, which captures shifting features and dirt from the lenses, contributes to 1.21% of the total variation. Although this is a low percentage, it still is a contributing factor that could aid in FFC. Together, the 4 principal components give $\sim$96% of the total variation.

A.4 Results: 2D radiation hydrodynamic simulation parameters

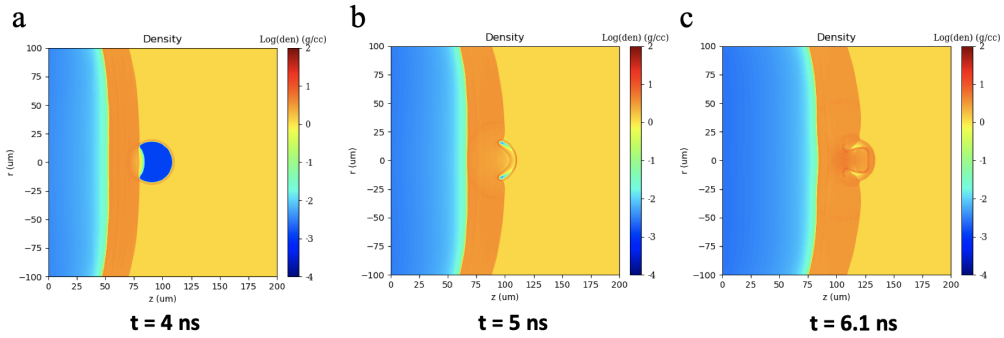

Figure A.3 Panels (a)-(c) are log scale density images. Panels (a) and (c) correspond to the same time steps as the experimental images in the main text. Panel (b) is included to show how we would expect the density to change with higher temporal resolution.

Here, we use 2D radiation hydrodynamic code to gain insight into material behavior at nanosecond and micron scales. Radiation transport and strength effects were neglected in our simulations and we chose specific parameters for this simulation to best match our experimental conditions. The parameters are listed in Table A.2.

The simulation in Fig. A.3 provided a model to help us understand void collapse evolution within the SU-8 medium on time scales comparable or shorter than the UXI camera. Each of these images are 2D slices of a 3D density map. Fig. A.3a and Fig. A.3c are the corresponding density maps associated with the experimental images in the main text. When the shock wave initially strikes the void in Fig. A.3a, the shock waves accelerates in the low density region, causing the wave in the void to move faster than the exterior shock wave. Fig. A.3b shows the density distribution if higher temporal resolution was obtained. Fig. A.3c shows when the shock wave nearly exits the

void and curl up starts to occur on the edges of the void. From this simulation we can visualize how the void alters the shock front propagation and density distribution near the void.

Table A.2 Simulation Parameters for 2D Hydro Code

Long-pulse laser energy	80J
Pulse type	flat-top
Pulse-duration	10 ns
Phase plate size	150 μm
SiO_2 void diameter	38 μm
SiO_2 void wall thickness	2 μm
SiO_2 density	2.2 g/cc
Void placement from epoxy edge	46 μm
SU-8 ablator thickness	400 μm
SU-8 density	1.2 g/cc
Kapton ablator thickness	25μm
Kapton ablator density	1.42 g/cc
Aluminum layer thickness	250 nm
Aluminum layer density	2.7 g/cc

Table A.2 displays the different parameters used in the 2D hydrodynamic simulations. These closely match the experimental conditions so the output of xRAGE can be used for qualitative comparison to our experimental images captured.

A.5 Analysis: Application of the transport-of-intensity (TIE) method

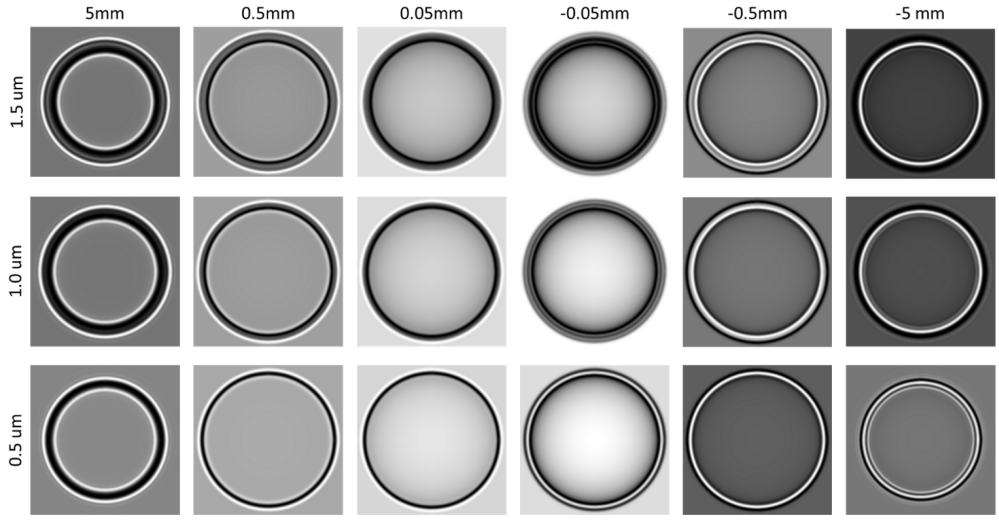

Figure A.4 XPCI simulations of the void for different SiO_2 thicknesses *t* (row) and L (column).

Fig. A.4 displays simulations of differing shell thicknesses *t* (row) and varying sample to detector distances *L* (column) for the hollow SiO_2 shell using the angular spectrum method. We compared the experimental data to the simulated images in Fig. A.4 and concluded that the presence of a distinct dark band with bright bands on either side of the void in the experimental data indicated that L$\geq$0 mm. After further analysis between the simulated and the experimental images, we deduced that the best value for *L* was +5 mm. This value was used for the TIE based phase retrieval approach to obtain mass density maps (areal density) of our sample undergoing laser shock compression. Additionally, this distance was used as the effective propagation distance for generating dynamic multi-frame void-shock XPCI simulations using phase and attenuation maps

calculated from xRAGE.

Bibliography

[1] J. Nuckolls, L. Wood, A. Thiessen, and G. Zimmerman, “Laser compression of matter to super-high densities: Thermonuclear (CTR) applications,” Nature 239 (1972).

[2] M. C. Herrmann, “Experimentally trained statistical models boost nuclear-fusion performance,” Nature 2021 565:7741 **565,** 577–578 (2019).

[3] V. A. Smalyuk *et al.*, “Recent and planned hydrodynamic instability experiments on indirect-drive implosions on the National Ignition Facility,” High Energy Density Physics 36 (2020).

[4] L. A. Pickworth *et al.*, “Visualizing deceleration-phase instabilities in inertial confinement fusion implosions using an "enhanced self-emission" technique at the National Ignition Facility,” Physics of Plasmas 25 (2018).

[5] S. W. Haan, H. Huang, M. A. Johnson, M. Stadermann, S. Baxamusa, S. Bhandarkar, D. S. Clark, V. Smalyuk, and H. F. Robey, “Instability growth seeded by oxygen in CH shells on the National Ignition Facility,” Physics of Plasmas 22 (2015).

[6] A. L. Kritcher *et al.*, "Comparison of plastic, high density carbon, and beryllium as indirect drive NIF ablators," Physics of Plasmas 25 (2018).

[7] S. J. Ali *et al.*, "Hydrodynamic instability seeding by oxygen nonuniformities in glow discharge polymer inertial fusion ablators," Physical Review E 98 (2018).

[8] A. B. Zylstra *et al.*, "Hot-spot mix in large-scale HDC implosions at NIF," Physics of Plasmas 27 (2020).

[9] H. Sio *et al.*, "Fuel–shell mix and yield degradation in kinetic shock-driven inertial confinement fusion implosions," Physics of Plasmas **29,** 072710 (2022).

[10] R. S. Craxton *et al.*, "Direct-drive inertial confinement fusion: A review," Physics of Plasmas **22,** 110501 (2015).

[11] D. Ranjan, J. Oakley, and R. Bonazza, "Shock-bubble interactions," Annual Review of Fluid Mechanics 43 (2011).

[12] A. W. Cook and D. Youngs, "Rayleigh-Taylor instability and mixing," Scholarpedia **4,** 6092 (2009), revision #91699.

[13] J. D. Kilkenny, S. G. Glendinning, and S. W. Haan, "A review of the ablative stabilization of the Rayleigh-Taylor instability in regimes relevant to inertial confinement fusion ARTICLES YOU MAY BE INTERESTED IN," Physics of Plasmas **1,** 1379 (1994).

[14] M. J. Andrews and D. B. Spalding, "A simple experiment to investigate two-dimensional mixing by Rayleigh-Taylor instability," Physics of Fluids A 2 (1990).

[15] Y. Zhou, "Rayleigh–Taylor and Richtmyer–Meshkov instability induced flow, turbulence, and mixing. II," Physics Reports **723,** 1–160 (2017).

[16] "Rayleigh-Taylor (RT) Image and Simulation,", http://large.stanford.edu/courses/2011/ph241/olson2/.

[17] T. Inoue, "Richtmyer-meshkov-type instability of a current sheet in a relativistically magnetized plasma," Astrophysical Journal 760 (2012).

[18] Y. Zhou, "A scaling analysis of turbulent flows driven by Rayleigh-Taylor and Richtmyer-Meshkov instabilities," Physics of Fluids 13 (2001).

[19] D. S. Clark *et al.*, "Radiation hydrodynamics modeling of the highest compression inertial confinement fusion ignition experiment from the National Ignition Campaign," Physics of Plasmas 22 (2015).

[20] D. L. Hill and S. I. Abarzhi, "On Rayleigh-Taylor and Richtmyer-Meshkov Dynamics With Inverse-Quadratic Power-Law Acceleration," Frontiers in Applied Mathematics and Statistics 7 (2022).

[21] F. Chen, A. Xu, and G. Zhang, "Collaboration and competition between Richtmyer-Meshkov instability and Rayleigh-Taylor instability," Physics of Fluids 30 (2018).

[22] NIF1.3MJ, "Fusion news ignites optimism," Nature Photonics 2021 15:10 **15,** 713–713 (2021).

[23] N. M. Hoffman *et al.*, "Measurement of areal density in the ablators of inertial-confinement-fusion capsules via detection of ablator (n, nγ) gamma-ray emission," Physics of Plasmas 20 (2013).

[24] M. Endrizzi, "X-ray phase-contrast imaging," Nuclear Instruments and Methods in Physics Research Section A: Accelerators, Spectrometers, Detectors and Associated Equipment **878,** 88–98 (2018).

[25] C. Bostedt, S. Boutet, D. M. Fritz, Z. Huang, H. J. Lee, H. T. Lemke, A. Robert, W. F. Schlotter, J. J. Turner, and G. J. Williams, "Linac Coherent Light Source: The first five years," Reviews of Modern Physics 88 (2016).

[26] J. P. Duris *et al.*, "Controllable X-Ray Pulse Trains from Enhanced Self-Amplified Spontaneous Emission," Physical Review Letters 126 (2021).

[27] B. W. McNeil and N. R. Thompson, "X-ray free-electron lasers," Nature photonics **4,** 814–821 (2010).

[28] N. Huang, H. Deng, B. Liu, D. Wang, and Z. Zhao, "Features and futures of X-ray free-electron lasers," The Innovation 2 (2021).

[29] "Working principle of a Free-Electron Laser,", https://nux.ethz.ch/research/x-ray-free-electron-laser-science.html.

[30] "Undulator Operation,", https://www-ssrl.slac.stanford.edu/stohr/xfels.pdf.

[31] F. J. Decker *et al.*, "A demonstration of multi-bunch operation in the LCLS," In *FEL 2010 - 32nd International Free Electron Laser Conference*, (2010).

[32] F. J. Decker *et al.*, "Tunable x-ray free electron laser multi-pulses with nanosecond separation," Scientific Reports 12 (2022).

[33] P. A. Hart *et al.*, "First x-ray test of the Icarus nanosecond-gated camera," https://doi.org/10.1117/12.2520974 **11038,** 31–39 (2019).

[34] S. Pandolfi *et al.*, "Novel Fabrication Tools for Dynamic Compression Targets with Engineered Voids Using Photolithography Methods," Review of Scientific Instruments (2022).

[35] D. Hodge *et al.*, "Four-frame ultrafast radiography of a shocked sample at an x-ray free electron laser," In *Optics InfoBase Conference Papers*, (2021).

[36] A. E. Gleason *et al.*, "Ultrafast visualization of crystallization and grain growth in shock-compressed SiO2," Nature Communications 6 (2015).

[37] E. E. McBride *et al.*, "Phase transition lowering in dynamically compressed silicon," Nature Physics 15 (2019).

[38] D. Kraus *et al.*, "Formation of diamonds in laser-compressed hydrocarbons at planetary interior conditions," Nature Astronomy 1 (2017).

[39] C. E. Wehrenberg *et al.*, "In situ X-ray diffraction measurement of shock-wave-driven twinning and lattice dynamics," Nature 550 (2017).

[40] B. Nagler *et al.*, "The Matter in Extreme Conditions instrument at the Linac Coherent Light Source," Journal of Synchrotron Radiation 22 (2015).

[41] S. Glenzer *et al.*, "Matter under extreme conditions experiments at the Linac Coherent Light Source," Journal of Physics B: Atomic, Molecular and Optical Physics **49,** 092001 (2016).

[42] E. Hurd, A. Carpenter, M. Dayton, C. Durand, S. Nagel, K. Engelhorn, L. Claus, and M. Sanchez, "Performance characterization of a four-frame nanosecond gated hybrid CMOS image sensor," In *Radiation Detectors in Medicine, Industry, and National Security XIX*, **10763,** 119–134 (2018).

[43] Y. Sun, F. J. Decker, J. Turner, S. Song, A. Robert, and D. Zhu, "Pulse intensity characterization of the LCLS nanosecond double-bunch mode of operation," Journal of Synchrotron Radiation 25 (2018).

[44] Y. Shi and D. W. Brenner, "Jetting and Detonation Initiation in Shock Induced Collapse of Nanometer-Scale Voids," Journal of Physical Chemistry C 112 (2008).

[45] "ALE3D Void Collapse Simulation,", https://wci.llnl.gov/simulation/computer-codes/ale3d.

[46] L. Claus, L. Fang, R. Kay, M. Kimmel, J. Long, G. Robertson, M. Sanchez, J. Stahoviak, D. Trotter, and J. L. Porter, "An overview of the Ultrafast X-ray Imager (UXI) program at Sandia Labs," In *Target Diagnostics Physics and Engineering for Inertial Confinement Fusion IV*, 9591 (2015).

[47] L. Claus, T. England, L. Fang, G. Robertson, M. Sanchez, D. Trotter, A. Carpenter, M. Dayton, P. Patel, and J. Porter, "Design and characterization of an improved, 2 ns, multi-frame imager for the Ultra-Fast X-ray Imager (UXI) program at Sandia National Laboratories," In *Target Diagnostics Physics and Engineering for Inertial Confinement Fusion VI*, **10390,** 16–26 (2017).

[48] H. Chen *et al.*, "A high-speed two-frame, 1-2 ns gated X-ray CMOS imager used as a hohlraum diagnostic on the National Ignition Facility (invited)," In *Review of Scientific Instruments*, 87 (2016).

[49] M. Dayton, A. Carpenter, H. Chen, N. Palmer, P. Datte, P. Bell, M. Sanchez, L. Claus, G. Robertson, and J. Porter, "A characterization technique for nanosecond gated CMOS x-ray cameras," In *Target Diagnostics Physics and Engineering for Inertial Confinement Fusion V*, 9966 (2016).

[50] D. Damiani *et al.*, "Linac Coherent Light Source data analysis using psana," Journal of Applied Crystallography 49 (2016).

[51] F. Krausz and M. Ivanov, "Attosecond physics," Reviews of Modern Physics 81 (2009).

[52] A. Criminisi, P. Pérez, and K. Toyama, "Region filling and object removal by exemplar-based image inpainting," IEEE Transactions on Image Processing 13 (2004).

[53] W. J. Carter and S. P. Marsh, "Hugoniot equation of state of polymers," Technical report, Los Alamos National Lab.(LANL), Los Alamos, NM (United States) (1995) .

[54] D. S. Hodge *et al.*, “Multi-frame, ultrafast, x-ray microscope for imaging shockwave dynamics,” Optics Express, Vol. 30, Issue 21, pp. 38405-38422 **30,** 38405–38422 (2022).

[55] R. Betti and O. Hurricane, “Inertial-confinement fusion with lasers,” Nature Physics **12,** 435–448 (2016).

[56] J. A. Gaffney, S. T. Brandon, K. D. Humbird, M. K. Kruse, R. C. Nora, J. L. Peterson, and B. K. Spears, “Making inertial confinement fusion models more predictive,” Physics of Plasmas 26 (2019).

[57] K. D. Humbird, J. L. Peterson, J. Salmonson, and B. K. Spears, “Cognitive simulation models for inertial confinement fusion: Combining simulation and experimental data,” Physics of Plasmas 28 (2021).

[58] V. A. Smalyuk *et al.*, “Hydrodynamic instability growth of three-dimensional, "native-roughness" modulations in x-ray driven, spherical implosions at the National Ignition Facility,” Physics of Plasmas 22 (2015).

[59] J. R. Peterson, B. M. Johnson, and S. W. Haan, “Instability growth seeded by DT density perturbations in ICF capsules,” Physics of Plasmas 25 (2018).

[60] V. A. Thomas and R. J. Kares, “Drive asymmetry and the origin of turbulence in an ICF implosion,” Physical Review Letters 109 (2012).

[61] B. M. Haines, J. P. Sauppe, B. J. Albright, W. S. Daughton, S. M. Finnegan, J. L. Kline, and J. M. Smidt, "A mechanism for reduced compression in indirectly driven layered capsule implosions," Physics of Plasmas **29,** 042704 (2022).

[62] Q. Looker, A. P. Colombo, M. Kimmel, and J. L. Porter, "X-ray characterization of the Icarus ultrafast x-ray imager," Review of Scientific Instruments 91 (2020).

[63] E. R. Hurd, T. Tate, M. S. Dayton, L. D. Claus, C. E. Durand, M. Johnston, J.-M. G. Di Nicola, A. C. Carpenter, and M. O. Sanchez, "Time Resolved Near Field (TRNF) diagnostic four-frame nanosecond gated hybrid CMOS image sensor," https://doi.org/10.1117/12.2525098 **11114,** 146–164 (2019).

[64] B. Nagler *et al.*, "The phase-contrast imaging instrument at the matter in extreme conditions endstation at LCLS," Review of Scientific Instruments 87 (2016).

[65] A. Aquila *et al.*, "The linac coherent light source single particle imaging road map," Structural Dynamics 2 (2015).

[66] A. Schropp *et al.*, "Full spatial characterization of a nanofocused X-ray free-electron laser beam by ptychographic imaging," Scientific Reports 3 (2013).

[67] A. Schropp *et al.*, "Imaging Shock Waves in Diamond with Both High Temporal and Spatial Resolution at an XFEL," Scientific Reports 5 (2015).

[68] J. Hagemann *et al.*, "Single-pulse phase-contrast imaging at free-electron lasers in the hard X-ray regime," Journal of Synchrotron Radiation 28 (2021).

[69] T. Vercauteren, X. Pennec, A. Perchant, and N. Ayache, “Non-parametric diffeomorphic image registration with the demons algorithm,” In *Lecture Notes in Computer Science (including subseries Lecture Notes in Artificial Intelligence and Lecture Notes in Bioinformatics)*, 4792 LNCS (2007).

[70] X. Pennec, P. Cachier, and N. Ayache, “Understanding the "demon’s algorithm": 3D non-rigid registration by gradient descent,” In *Lecture Notes in Computer Science (including subseries Lecture Notes in Artificial Intelligence and Lecture Notes in Bioinformatics)*, 1679 (1999).

[71] D. Paganin, S. C. Mayo, T. E. Gureyev, P. R. Miller, and S. W. Wilkins, “Simultaneous phase and amplitude extraction from a single defocused image of a homogeneous object,” Journal of Microscopy 206 (2002).

[72] M. Beltran, D. Paganin, K. Uesugi, and M. Kitchen, “2D and 3D X-ray phase retrieval of multi-material objects using a single defocus distance,” Optics Express 18 (2010).

[73] J. M. Shaw, J. D. Gelorme, N. C. LaBianca, W. E. Conley, and S. J. Holmes, “Negative photoresists for optical lithography,” IBM Journal of Research and Development 41 (1997).

[74] I. Roch, P. Bidaud, D. Collard, and L. Buchaillot, “Fabrication and characterization of an SU-8 gripper actuated by a shape memory alloy thin film,” Journal of Micromechanics and Microengineering 13 (2003).

[75] S. Marsh, *LASL Shock Hugoniot Data* (University of California Press, 1980).

[76] P. Emma *et al.*, "First lasing and operation of an ångstrom-wavelength free-electron laser," Nature Photonics 4 (2010).

[77] B. Pfau and S. Eisebitt, "X-ray holography," in *Synchrotron Light Sources and Free-Electron Lasers: Accelerator Physics, Instrumentation and Science Applications* (2020).

[78] S. C. Mayo, A. W. Stevenson, and S. W. Wilkins, "In-Line Phase-Contrast X-ray Imaging and Tomography for Materials Science," Materials 5 (2012).

[79] E. Pagot, P. Cloetens, S. Fiedler, A. Bravin, P. Coan, J. Baruchel, J. Härtwig, and W. Thomlinson, "A method to extract quantitative information in analyzer-based x-ray phase contrast imaging," Applied Physics Letters 82 (2003).

[80] A. Momose, "Phase-sensitive imaging and phase tomography using X-ray interferometers," Optics Express 11 (2003).

[81] S. B. Brown *et al.*, "Direct imaging of ultrafast lattice dynamics," Science Advances 5 (2019).

[82] S. V. Milton *et al.*, "Exponential gain and saturation of a self-amplified spontaneous emission free-electron laser," Science 292 (2001).

[83] K. Buakor, Y. Zhang, Š. Birnšteinová, V. Bellucci, T. Sato, H. Kirkwood, A. P. Mancuso, P. Vagovic, and P. Villanueva-Perez, "Shot-to-shot flat-field correction at X-ray free-electron lasers," Optics Express 30 (2022).

[84] I. T. Jolliffe and J. Cadima, "Principal component analysis: a review and recent developments," Philosophical Transactions of the Royal Society A: Mathematical, Physical and Engineering Sciences **374,** 20150202 (2016).

[85] J. Shlens, "A tutorial on principal component analysis," arXiv preprint arXiv:1404.1100 (2014).

[86] L. I. Smith, "A tutorial on Principal Components Analysis Introduction," Statistics (2002).

[87] M. Gittings *et al.*, "The RAGE radiation-hydrodynamic code," Computational Science and Discovery 1 (2008).

[88] M. A. Barrios, D. G. Hicks, T. R. Boehly, D. E. Fratanduono, J. H. Eggert, P. M. Celliers, G. W. Collins, and D. D. Meyerhofer, "High-precision measurements of the equation of state of hydrocarbons at 1-10 Mbar using laser-driven shock waves," In *Physics of Plasmas*, 17 (2010).

[89] C. G. Schroer *et al.*, "High resolution imaging and lithography with hard x rays using parabolic compound refractive lenses," In *Review of Scientific Instruments*, 73 (2002).

[90] T. Weitkamp, C. Rau, A. A. Snigirev, B. Benner, T. F. Guenzler, M. Kuhlmann, and C. G. Schroer, "In-line phase contrast in synchrotron-radiation microradiography and tomography," In *Developments in X-Ray Tomography III*, 4503 (2002).

[91] V. Kohn, I. Snigireva, and A. Snigirev, "Diffraction theory of imaging with X-ray compound refractive lens," Optics Communications 216 (2003).

[92] V. G. Kohn, "An exact theory of imaging with a parabolic continuously refractive X-ray lens," Journal of Experimental and Theoretical Physics 97 (2003).

[93] D. Paganin *et al.*, *Coherent X-ray optics* (Oxford University Press on Demand, 2006), No. 6.

[94] D. M. Paganin, V. Favre-Nicolin, A. Mirone, A. Rack, J. Villanova, M. P. Olbinado, V. Fernandez, J. C. da Silva, and D. Pelliccia, "Boosting spatial resolution by incorporating periodic boundary conditions into single-distance hard-x-ray phase retrieval," Journal of Optics (United Kingdom) 22 (2020).

[95] H. K. Chung, M. H. Chen, W. L. Morgan, Y. Ralchenko, and R. W. Lee, "FLYCHK: Generalized population kinetics and spectral model for rapid spectroscopic analysis for all elements," High Energy Density Physics 1 (2005).

[96] I. Häggmark, W. Vågberg, H. M. Hertz, and A. Burvall, "Comparison of quantitative multi-material phase-retrieval algorithms in propagation-based phase-contrast X-ray tomography," Optics Express 25 (2017).

[97] J. Miao, T. Ishikawa, I. K. Robinson, and M. M. Murnane, "Beyond crystallography: Diffractive imaging using coherent x-ray light sources," Science **348,** 530–535 (2015).

[98] D. Sayre, "Some implications of a theorem due to Shannon," Acta Crystallographica 5 (1952).

[99] Y. Shechtman, Y. C. Eldar, O. Cohen, H. N. Chapman, J. Miao, and M. Segev, "Phase retrieval with application to optical imaging: a contemporary overview," IEEE signal processing magazine **32,** 87–109 (2015).

[100] Y. H. Lo, L. Zhao, M. Gallagher-Jones, A. Rana, J. Lodico, W. Xiao, B. C. Regan, and J. Miao, "In situ coherent diffractive imaging," Nature Communications 9 (2018).

[101] R. L. Sandberg, "Closing the Gap to the Diffraction Limit: Near Wavelength Limited Tabletop Soft X-Ray Coherent Diffractive Imaging," Physics **PhD,** 147 (2009).

[102] J. R. Fienup, "Phase retrieval algorithms: a comparison," Applied Optics 21 (1982).

[103] J. R. Fienup, "Reconstruction of an object from the modulus of its Fourier transform," Optics Letters 3 (1978).

[104] Y. Gao and L. Cao, "Generalized optimization framework for pixel super-resolution imaging in digital holography," Optics Express 29 (2021).

[105] J. Miao, D. Sayre, and H. N. Chapman, "Phase retrieval from the magnitude of the Fourier transforms of nonperiodic objects," Journal of the Optical Society of America A 15 (1998).

[106] J. Miao, J. Kirz, and D. Sayre, "The oversampling phasing method," Acta Crystallographica Section D: Biological Crystallography 56 (2000).

[107] J. Miao, T. Ishikawa, E. H. Anderson, and K. O. Hodgson, "Phase retrieval of diffraction patterns from noncrystalline samples using the oversampling method," Physical Review B - Condensed Matter and Materials Physics 67 (2003).

[108] C. C. Chen, J. Miao, C. W. Wang, and T. K. Lee, "Application of optimization technique to noncrystalline x-ray diffraction microscopy: Guided hybrid input-output method," Physical Review B - Condensed Matter and Materials Physics 76 (2007).

[109] S. Marchesini, H. He, N. Chapman, P. Hau-Riege, A. Noy, R. Howells, U. Weierstall, and H. Spence, "X-ray image reconstruction from a diffraction pattern alone," Physical Review B - Condensed Matter and Materials Physics 68 (2003).

[110] S. Marchesini, "Invited article: A unified evaluation of iterative projection algorithms for phase retrieval (vol 78, art no 011301, 2007)," Review of Scientific Instruments 78 (2007).

[111] A. M. Maiden and J. M. Rodenburg, "An improved ptychographical phase retrieval algorithm for diffractive imaging," Ultramicroscopy 109 (2009).

[112] A. Maiden, D. Johnson, and P. Li, "Further improvements to the ptychographical iterative engine," Optica 4 (2017).

[113] D. R. Luke, J. V. Burke, and R. G. Lyon, "Optical wavefront reconstruction: Theory and numerical methods," SIAM Review 44 (2002).

[114] B. Abbey, K. A. Nugent, G. J. Williams, J. N. Clark, A. G. Peele, M. A. Pfeifer, M. De Jonge, and I. McNulty, "Keyhole coherent diffractive imaging," Nature Physics 4 (2008).

[115] P. Thibault and I. C. Rankenburg, "Optical diffraction microscopy in a teaching laboratory," American Journal of Physics 75 (2007).

[116] P. Thibault, M. Dierolf, O. Bunk, A. Menzel, and F. Pfeiffer, "Probe retrieval in ptychographic coherent diffractive imaging," Ultramicroscopy 109 (2009).

[117] J. A. Rodriguez, R. Xu, C. C. Chen, Y. Zou, and J. Miao, "Oversampling smoothness: An effective algorithm for phase retrieval of noisy diffraction intensities," Journal of Applied Crystallography 46 (2013).

[118] F. Momey, L. Denis, T. Olivier, and C. Fournier, "From Fienup's phase retrieval techniques to regularized inversion for in-line holography: tutorial," Journal of the Optical Society of America A 36 (2019).

[119] R. W. Gerchberg and W. O. Saxton, "PRACTICAL ALGORITHM FOR THE DETERMINATION OF PHASE FROM IMAGE AND DIFFRACTION PLANE PICTURES.," Optik (Stuttgart) 35 (1972).

[120] J. R. Fienup, T. R. Crimmins, and W. Holsztynski, "RECONSTRUCTION OF THE SUPPORT OF AN OBJECT FROM THE SUPPORT OF ITS AUTOCORRELATION.," Journal of the Optical Society of America 72 (1982).

[121] J. R. Fienup and C. C. Wackerman, "Phase-retrieval stagnation problems and solutions," Journal of the Optical Society of America A 3 (1986).

[122] J. R. Fienup, "Reconstruction of a complex-valued object from the modulus of its Fourier transform using a support constraint," Journal of the Optical Society of America A 4 (1987).

[123] B. Shi, Q. Lian, X. Huang, and N. An, "Constrained phase retrieval: when alternating projection meets regularization," Journal of the Optical Society of America B 35 (2018).

[124] M. Pham, P. Yin, A. Rana, S. Osher, and J. Miao, "Generalized proximal smoothing (GPS) for phase retrieval," Optics Express 27 (2019).

[125] V. Elser, "Phase retrieval by iterated projections," Journal of the Optical Society of America A 20 (2003).

[126] M. A. Pfeifer, G. J. Williams, I. A. Vartanyants, R. Harder, and I. K. Robinson, "Three-dimensional mapping of a deformation field inside a nanocrystal," Nature 442 (2006).

[127] C. Shen, X. Bao, J. Tan, S. Liu, and Z. Liu, "Two noise-robust axial scanning multi-image phase retrieval algorithms based on Pauta criterion and smoothness constraint," Optics Express 25 (2017).

[128] M. J. Sun and J. M. Zhang, "Phase retrieval utilizing geometric average and stochastic perturbation," Optics and Lasers in Engineering 120 (2019).

[129] B. Li, O. K. Ersoy, C. Ma, Z. Pan, W. Wen, Z. Song, and W. Gao, "Phase retrieval based on difference map and deep neural networks," Journal of Modern Optics 68 (2021).

[130] D. E. Adams, L. S. Martin, M. D. Seaberg, D. F. Gardner, H. C. Kapteyn, and M. M. Murnane, "A generalization for optimized phase retrieval algorithms," Optics Express 20 (2012).

[131] P. Sidorenko and O. Cohen, "Single-shot ptychography," Optica 3 (2016).

[132] E. J. Candès, X. Li, and M. Soltanolkotabi, “Phase retrieval via wirtinger flow: Theory and algorithms,” IEEE Transactions on Information Theory 61 (2015).

[133] Y. Gao, F. Yang, and L. Cao, “Pixel Super-Resolution Phase Retrieval for Lensless On-Chip Microscopy via AcceleratedWirtinger Flow,” MDPI (2022).

[134] C. Guo, X. Liu, F. Zhang, Y. Du, S. Zheng, Z. Wang, X. Zhang, X. Kan, Z. Liu, and W. Wang, “Lensfree on-chip microscopy based on single-plane phase retrieval,” Optics Express (2022).

[135] H. Li, X. Chen, Z. Chi, C. Mann, and A. Razi, “Deep DIH: Single-Shot Digital In-Line Holography Reconstruction by Deep Learning,” IEEE Access 8 (2020).

[136] F. Niknam, H. Qazvini, and H. Latifi, “Holographic optical field recovery using a regularized untrained deep decoder network,” Scientific Reports 11 (2021).

[137] D. Yang, J. Zhang, Y. Tao, W. Lv, S. Lu, H. Chen, W. Xu, and Y. Shi, “Dynamic coherent diffractive imaging with a physics-driven untrained learning method,” Optics Express 29 (2021).

[138] K. A. Nugent, “X-ray noninterferometric phase imaging: a unified picture,” Journal of the Optical Society of America A 24 (2007).

[139] A. Burvall, U. Lundström, P. A. C. Takman, D. H. Larsson, and H. M. Hertz, “Phase retrieval in X-ray phase-contrast imaging suitable for tomography,” Optics Express 19 (2011).

[140] T. Latychevskaia and H. W. Fink, “Solution to the twin image problem in holography,” Physical Review Letters 98 (2007).

[141] T. Latychevskaia and H.-W. Fink, “Reconstruction of purely absorbing, absorbing and phase-shifting, and strong phase-shifting objects from their single-shot in-line holograms,” Applied Optics 54 (2015).